The Astrophysical Journal, 976:88 (18pp), 2024 November 20 https://doi.org/10.3847/1538-4357/ad758c

Disk Turbulence and Star Formation Regulation in High-z Main-sequence Analog Galaxies

Laura Lenkić[1,2,3], Deanne B. Fisher[4,5], Alberto D. Bolatto[1], Peter J. Teuben[1], Rebecca C. Levy[6,11], Jiayi Sun[7,12], Rodrigo Herrera-Camus[8], Karl Glazebrook[4,5], Danail Obreschkow[9], and Roberto Abraham[10]
[1] Department of Astronomy, University of Maryland, College Park, MD 20742, USA; laura.lenkic@gmail.com
[2] SOFIA Science Center, USRA, NASA Ames Research Center, M.S. N232-12, Moffett Field, CA 94035, USA
[3] Jet Propulsion Laboratory, California Institute of Technology, 4800 Oak Grove Drive, Pasadena, CA 91109, USA
[4] Centre for Astrophysics and Supercomputing, Swinburne University of Technology, PO Box 218, Hawthorn, VIC 3122, Australia
[5] ARC Centre of Excellence for All Sky Astrophysics in 3 Dimensions (ASTRO 3D), Australia
[6] Steward Observatory, University of Arizona, Tucson, AZ 85721, USA
[7] Department of Astrophysical Sciences, Princeton University, 4 Ivy Lane, Princeton, NJ 08544, USA
[8] Departamento de Astronomía, Universidad de Concepción, Barrio Universitario, Concepción, Chile
[9] International Centre for Radio Astronomy Research (ICRAR), University of Western Australia, Crawley, WA 6009, Australia
[10] Department of Astronomy & Astrophysics, University of Toronto, 50 St. George Street, Toronto, ON M5S 3H4, Canada
Received 2023 December 14; revised 2024 July 22; accepted 2024 August 4; published 2024 November 14

Abstract

The gas-phase velocity dispersions in disk galaxies, which trace turbulence in the interstellar medium, are observed to increase with lookback time. However, the mechanisms that set this rise in turbulence are observationally poorly constrained. To address this, we combine kiloparsec-scale Atacama Large Millimeter/submillimeter Array observations of CO(3−2) and CO(4−3) with Hubble Space Telescope observations of Hα to characterize the molecular gas and star formation properties of seven local analogs of main-sequence galaxies at $z \sim 1$–2, drawn from the DYNAMO sample. Investigating the "molecular gas main sequence" on kiloparsec scales, we find that galaxies in our sample are more gas-rich than local star-forming galaxies at all disk positions. We measure beam-smearing-corrected molecular gas velocity dispersions and relate them to the molecular gas and star formation rate surface densities. Despite being relatively nearby ($z \sim 0.1$), DYNAMO galaxies exhibit high velocity dispersions and gas and star formation rate surface densities throughout their disks, when compared to local star-forming samples. Comparing these measurements to predictions from star formation theory, we find very good agreements with the latest feedback-regulated star formation models. However, we find that theories that combine dissipation of gravitational energy from radial gas transport with feedback overestimate the observed molecular gas velocity dispersions.

Unified Astronomy Thesaurus concepts: Stellar feedback (1602); Star formation (1569); Starburst galaxies (1570); Disk galaxies (391)

1. Introduction

A key result of large numbers of surveys over the past decade is the rise in gas-phase velocity dispersions from the local Universe to those galaxies at lookback times of ∼10 billion years ($z \sim 2$; e.g., D. R. Law et al. 2009; N. M. Förster Schreiber et al. 2011; R. Genzel et al. 2011; B. Epinat et al. 2012; S. A. Kassin et al. 2012; E. Wisnioski et al. 2015; H. Übler et al. 2019). This evolution of velocity dispersion is correlated with increases in many physical properties of galaxies, especially those related to star formation and the interstellar medium (ISM). Galaxies of a fixed stellar mass show increases in molecular gas surface density, star formation rate surface density, and gas fraction with lookback time (see reviews by K. Glazebrook 2013; L. J. Tacconi et al. 2020; N. M. Förster Schreiber & S. Wuyts 2020). They also become more compact and their morphologies become dominated by patches of high star formation, typically called clumps. Understanding what mechanisms set the rise in velocity dispersion in disk galaxies, and how it is linked to other changes in the ISM, is therefore needed to build accurate models of galaxy evolution. A historical challenge to this has been the lack of resolved observations of the cold gas velocity dispersions in galaxies with higher gas fractions ($f_{\rm gas} > 15\%$) and clumpy morphologies.

The observed velocity dispersion in disks is typically interpreted to reflect the turbulence of gas in the ISM. Turbulence is a key mechanism to help galaxies regulate their star formation (F. Bournaud et al. 2010). In many theories, the gas collapse induced by the gravitational potential well of gas, stars, and dark matter is balanced by the thermal, turbulent, radiation, and magnetic pressures, where turbulence is often invoked as the primary balancing force. An important question in understanding this equilibrium state is determining what mechanisms predominantly drive turbulence in the ISM. Under the theory of self-regulated star formation, momentum injected by stellar feedback is enough to drive the turbulence needed to balance the vertical weight of the ISM (R. Shetty & E. C. Ostriker 2012; C.-A. Faucher-Giguere et al. 2013). Alternatively, theories of gas dynamics predict that the accretion-powered release of gravitational potential energy via radial inflows of gas through a galactic disk is the primary driver of turbulence (M. R. Krumholz & B. Burkhart 2016) or that both stellar feedback and gas transport are required to explain observations of the relation between velocity dispersion

[11] NSF Astronomy and Astrophysics Postdoctoral Fellow.
[12] NASA Hubble Fellow.

and star formation rate surface density (B. G. Elmegreen & A. Burkert 2010; R. S. Klessen & P. Hennebelle 2010; M. R. Krumholz et al. 2018).

An important, recent advancement in this area is the increasing number of observations of velocity dispersion in cold gas tracers. Recent work finds that CO-based measurements of the velocity dispersion are systematically lower than those using ionized gas tracers (R. C. Levy et al. 2018; H. Übler et al. 2019; M. Girard et al. 2019, 2021; D. Liu et al. 2023). Typical differences between the measured velocity dispersion in ions and molecules can be quite high, $\sigma_{\rm ion} - \sigma_{\rm mol} \sim 30$–$50$ km s^{-1}. M. Girard et al. (2021) compiled a sample of galaxies and showed that the offset is a roughly constant ratio, $\sigma_{\rm ion}/\sigma_{\rm mol} \sim 2$–$3$, with respect to gas fraction and redshift, while H. Übler et al. (2019) argued that the offset may evolve, becoming smaller at higher redshift. However, there are not sufficient data points at higher redshift to conclusively determine whether $\sigma_{\rm ion}/\sigma_{\rm mol}$ evolves with redshift or not. Nevertheless, there appears to be agreement overall that this offset exists and is significantly larger than a simple correction for the thermal broadening of H II regions, which is rarely more than 15 km s^{-1} (M. R. Krumholz & B. Burkhart 2016).

Molecular gas represents a significantly larger fraction of the ISM mass than ions, and thus may be more representative of turbulence in galaxies, especially the part that is involved in regulating star formation. M. Girard et al. (2021) showed that this difference has important implications for comparison to theory, and found that models of gravity+feedback overestimate the velocity dispersion when measured with CO. Recent simulations found similar results: feedback acts to stratify the gas disk and generates differences in the velocity dispersion of ionized and molecular gas (T. Ejdetjarn et al. 2022; T.-E. Rathjen et al. 2023).

Gas velocity dispersion is not the only means of studying the regulation of star formation in galaxies. The Kennicutt–Schmidt relation (hereafter KS relation; M. Schmidt 1959; R. C. Kennicutt 1998; R. C. Kennicutt & N. J. Evans 2012), which ties the surface density of star formation ($\Sigma_{\rm SFR}$) to the surface density of gas ($\Sigma_{\rm mol}$) through a power-law relation with a slope of $N \sim 1.4$, is a widely studied relationship that is discussed in many of the theories described above. It is frequently used as a basic metric of how rapidly gas is consumed by star formation. The KS relation spans several orders of magnitude in both the star formation rate (SFR) and gas surface density, and it holds for both normal star-forming galaxies and starbursting systems (R. C. Kennicutt & M. A. C. De Los Reyes 2021).

A strong relationship between $\Sigma_{\rm SFR}$ and $\Sigma_{\rm mol}$ appears to persist on ∼1 kpc scales (A. K. Leroy et al. 2008; S. F. Sánchez et al. 2021), though subtle differences in the slope of the relation may exist. A large number of authors studying spirals in the local Universe argue for slopes that are close to unity (F. Bigiel et al. 2008; A. K. Leroy et al. 2013; J. Sun et al. 2023). At $z \sim 1$–2 the picture is far less clear. Only a handful of galaxies have resolved observations of both $\Sigma_{\rm SFR}$ and $\Sigma_{\rm mol}$. As recently discussed by D. B. Fisher et al. (2022), the combined sample of targets from the literature is quite heterogeneous, hindering our ability to derive any general conclusions about the nature of this relationship at high $\Sigma_{\rm SFR}$. Systematic studies of selected samples of galaxies measuring the resolved KS relation at $z > 0.5$ remain absent from the literature (see discussion by L. J. Tacconi et al. 2020).

In this paper, we study the molecular gas velocity dispersions ($\sigma_{\rm mol}$), molecular gas surface densities ($\Sigma_{\rm mol}$), and star formation rate surface densities ($\Sigma_{\rm SFR}$) of seven highly turbulent, nearby ($z \sim 0.1$) galaxies from the Dynamics of Newly Assembled Massive Objects (DYNAMO; A. W. Green et al. 2014) sample. The gas fractions (D. B. Fisher et al. 2014; H. A. White et al. 2017) and ionized gas velocity dispersions (A. W. Green et al. 2014; P. Oliva-Altamirano et al. 2018) of these galaxies are most consistent with main-sequence star-forming galaxies at $z \sim 1$. Moreover, the Hα morphology is consistent with so-called "clumpy" galaxies (D. B. Fisher et al. 2017b; L. Lenkic et al. 2021; L. Ambachew et al. 2022). Furthermore, the star formation rates and stellar masses of DYNAMO galaxies place them on the main sequence of star formation at $z \sim 2$ rather than the local ($z \sim 0.1$) one (D. B. Fisher et al. 2019). Their resemblance to high-redshift systems and proximity to us allows us to probe the turbulence-powering mechanisms in gas-rich galaxies on kiloparsec scales.

We combine Hα observations from the Hubble Space Telescope (HST) with CO(3−2) and CO(4−3) observations from the Atacama Large Millimeter/submillimeter Array (ALMA) to study the $\sigma_{\rm mol}$−$\Sigma_{\rm mol}$ and $\sigma_{\rm mol}$−$\Sigma_{\rm SFR}$ relations resolved on ∼1–2 kpc scales, and compare these to results from simulations and expectations from star formation theory. This paper is structured as follows: Section 2 describes our observations and data reduction, Section 3 describes how we derive molecular gas surface density, star formation rate surface density, stellar mass surface density, and velocity dispersions, Section 4 presents our results on the "molecular gas main sequence," KS relation, and the $\sigma_{\rm mol}$−$\Sigma_{\rm mol}$ and $\sigma_{\rm mol}$−$\Sigma_{\rm SFR}$ relations, Section 5 compares our results to expectations from theories of star formation regulation, and finally we conclude in Section 6.

Throughout this work, we assume ΛCDM cosmology with $H_0 = 69.6$ km s^{-1}, $\Omega_m = 0.286$, and $\Omega_\Lambda = 0.714$, and a Kroupa initial mass function (P. Kroupa 2001).

2. Observations

2.1. Galaxy Sample

The DYNAMO sample was first defined by A. W. Green et al. (2014), who selected galaxies from the MPA-JHU Value Added Catalog of the Sloan Digital Sky Survey based on their redshifts and Hα emissions. The sample comprises 67 galaxies, of which half have $L_{\rm H\alpha} > 10^{42}$ erg s^{-1}. A significant amount of previous work has compared DYNAMO to $z \sim 1$ systems. DYNAMO galaxies, including those studied in this work, have been shown to be much more gas-rich than galaxies in the local Universe, with gas fractions of order 10%–70% (D. B. Fisher et al. 2014, 2019; H. A. White et al. 2017). This is higher than main-sequence galaxies in the local Universe by roughly a factor of a few (A. Saintonge et al. 2011), and similar to galaxies at $z \sim 1$ (L. J. Tacconi et al. 2020). DYNAMO galaxies have likewise been shown to be clumpy in both ionized gas (D. B. Fisher et al. 2017b) and *U*-band starlight (L. Lenkic et al. 2021; L. Ambachew et al. 2022), where clumps are defined as done in the CANDELS survey using the ratio of clump light to total galaxy light (Y. Guo et al. 2015).

The kinematics of DYNAMO galaxies are similar to those of $z \sim 1$ galaxies in more ways than simply the velocity dispersion. D. B. Fisher et al. (2017a) show that DYNAMO galaxies are consistent with low values of Toomre *Q*, $Q \sim 0.5$–1.5 (see also H. A. White et al. 2017) and that the Toomre values correlate to

Table 1
Galaxy properties

Galaxy	z	M_* ($10^{10}\,M_\odot$)	SFR ($M_\odot$ yr^{-1})	$f_{\rm gas}$ [a]	$\sigma_{0,\rm ion}$ [b] (km s^{-1})	$\sigma_{0,\rm mol}$ [b] (km s^{-1})	$\sigma_{m,\rm mol}$ [c] (km s^{-1})	$\Sigma_{\rm SFR}$ [a] ($\log(M_\odot\ {\rm yr}^{-1}\ {\rm kpc}^{-2})$)	CO Beam FWHM (kpc (arcsec))
C13-1	0.07876	3.58	5.06 ± 0.5	0.06 ± 0.02	26	8	17	-1.64 ± 0.05	1.60 (1.07)
D13-5	0.07535	5.38	17.48 ± 0.45	0.36 ± 0.02	40	12	22	-0.48 ± 0.02	1.58 (1.10)
D15-3	0.06712	5.42	8.29 ± 0.35	0.17 ± 0.04	25	8	14	-0.87 ± 0.03	1.24 (0.96)
G04-1	0.12981	6.47	21.32 ± 1	0.33 ± 0.04	30	13	16	-0.65 ± 0.03	0.98 (0.42)
G08-5	0.13217	1.73	10.04 ± 1	0.30 ± 0.05	36	15	20	-0.63 ± 0.04	0.95 (0.40)
G14-1	0.13233	2.23	6.9 ± 0.5	0.77 ± 0.08	71	27	35	-0.36 ± 0.04	1.02 (0.43)
G20-2	0.14113	2.16	18.24 ± 0.35	0.21 ± 0.05	36	9	23	-0.48 ± 0.02	3.08 (1.23)

Notes.
[a] Values from D. B. Fisher et al. (2017b, 2019) and H. A. White et al. (2017).
[b] Values from M. Girard et al. (2021). Uncertainty on the ionized gas velocity dispersion, $\sigma_{0,\rm ion}$, is 3–5 km s^{-1}, and on the molecular gas velocity dispersion, $\sigma_{0,\rm mol}$, is 2–3 km s^{-1}.
[c] The median velocity dispersion in this work determined by fitting each line-of-sight CO line profile with a Gaussian and correcting for beam smearing is given by $\sigma_{m,\rm mol}$.

the clump sizes. D. Obreschkow et al. (2015) show that DYNAMO galaxies are low-angular-momentum outliers to local relationships between specific angular momentum (j) and galaxy mass. They have j/M_* that is more similar to observations at $z \sim 1$. Overall, DYNAMO galaxies have been shown in many ways to have similar properties to $z \sim 1$ galaxies.

In this work, we use seven targets from the intersection of the samples of D. B. Fisher et al. (2017b), which provides HST imaging of DYNAMO targets, and L. Lenkić et al. (2023), which provides ALMA CO maps for the same galaxies. In Table 1, we summarize the basic properties of the galaxies in this paper.

2.2. ALMA and HST Observations

The ALMA observations we use are associated with project codes 2017.1.00239.S (PI: D. B. Fisher) and 2019.1.00447.S (PI: R. Herrera-Camus). These observations were imaged using `tclean` with the Common Astronomy Software Application (CASA, J. P. McMullin et al. 2007) with `weighting=''briggs''` and `robust=0.5`. Detailed information on the data processing and data products can be found in L. Lenkić et al. (2023).

In addition to the ALMA observations of CO in our DYNAMO galaxies, we make use of HST observations of Hα as a tracer of the star formation rate (PID 12977; P.I.: I. Damjanov), and HST WFC3/IR F125W observations ($\sim J$ band) as a tracer of the stellar mass (PID 15069; P.I.: D. B. Fisher). For details of the reduction and analysis of these observations, see D. B. Fisher et al. (2017b) and L. Ambachew et al. (2022), respectively.

To investigate the kiloparsec-scale KS relation and the relation between $\sigma_{\rm mol}$ and $\Sigma_{\rm mol}$ and $\Sigma_{\rm SFR}$, we match the pixel scale and resolution of the Hα and F125W observations to those of the CO(3−2) where available, and CO(4−3) otherwise. To achieve this, we convolve the HST observations with a two-dimensional Gaussian function whose FWHM is equal to the circularized beam of the corresponding ALMA observation. Then, we reproject and regrid them to match the world coordinate system information and pixel scale of the CO observations using the PYTHON ASTROPY package `reproject`,[13] which assumes input images have surface brightness units. Our input images have count rate units, thus we scale the reprojected images by the squared ratio of the new pixel scale and old pixel scale to conserve flux.

[13] https://reproject.readthedocs.io/en/stable/index.html

3. Methods

The properties we are interested in measuring and studying are: (1) the stellar mass surface densities (Σ_*), (2) the molecular gas surface density ($\Sigma_{\rm mol}$) adopting both a constant and a variable CO-to-H$_2$ conversion factor ($\alpha_{\rm CO}$), (3) the SFR surface density ($\Sigma_{\rm SFR}$), and (4) the molecular gas velocity dispersions ($\sigma_{\rm mol}$).

For each data set, we define a "grid" of circular, beam-sized apertures centered on the galaxy, and a second that is offset from the center by 0.5× the beam FWHM in both the x- and y-directions (R.A. and decl.) to cover the gaps in the first grid.

3.1. Stellar Mass Surface Density

We measure the stellar mass surface density (Σ_*) from HST F125W observations, matched to the resolution and pixel scale of the CO observations. We perform aperture photometry along every beam-sized line of sight in the two grids, as described above. In addition, we perform aperture photometry in the same way on HST WFC3/UVIS F336W observations and then measure the F336W − F125W color. L. Ambachew et al. (2022) studied the stellar masses of clumps in a sample of DYNAMO galaxies and derived mass-to-light ratios based on HST colors. Therefore, we use the F336W − F125W colors we measure to derive a mass-to-light ratio ($\Upsilon_{*,\rm F125W}$) for each line-of-sight beam-sized aperture from the relation

$$\log \Upsilon_{*,\rm F125W} = 0.195 \times ({\rm F336W} - {\rm F125W}) - 1.187 \quad (1)$$

and we impose a floor of $\log \Upsilon_{*,\rm F125W} = -1$.

However, no F336W or F125W observations for DYNAMO C13-1 were available; thus, we use HST ACS/WFC FR647M instead and derive the masses from

$$\log M_* = \log(F_{\rm FR647M}\ [{\rm Jy\ cm^2}]) - 42.04. \quad (2)$$

3.2. Molecular Gas Surface Density

We measure the molecular gas surface density from our integrated intensity maps of CO(3−2) in all cases but DYNAMO D15-3, for which no CO(3−2) was available. In that case, we use the CO(4−3) integrated intensity map. For

each beam-sized aperture in our "grid," we extract the median integrated intensity of all pixels within the aperture and calculate the molecular gas surface density from

$$\Sigma_{\rm mol} = \alpha_{\rm CO} \times R_{J,J-1} \times I_{\rm CO}[M_\odot\ {\rm pc}^{-2}] \quad (3)$$

where $R_{J,J-1}$ is the conversion of the CO($J \rightarrow J-1$) emission to CO(1−0), for which we adopt the R_{31} and R_{41} values in Table 3 of L. Lenkić et al. (2023), and $I_{\rm CO}$ is the CO($J \rightarrow J-1$) integrated intensity in units of K km s^{-1}.

In the case of a constant CO-to-H_2 conversion factor, we adopt $\alpha_{\rm CO} = 4.35\ M_\odot\ ({\rm K\ km\ s^{-1}\ pc^2})^{-1}$, which represents the average value for a Milky Way–like galaxy (e.g., A. D. Bolatto et al. 2013). In the case of variable $\alpha_{\rm CO}$, we adopt the prescription of A. D. Bolatto et al. (2013) in their Equation (31):

$$\alpha_{\rm CO} \sim 2.9 \times \exp\left(\frac{0.4}{Z'\,\Sigma_{\rm GMC}^{100}}\right) \times \left(\frac{\Sigma_{\rm total}}{100\ M_\odot\ {\rm pc}^{-2}}\right)^{\gamma} \quad (4)$$

where Z' is the metallicity normalized to the solar value, $\Sigma_{\rm GMC}^{100}$ is the gas surface density in units of $100\ M_\odot\ {\rm pc}^{-2}$, $\Sigma_{\rm total}$ is the gas plus stellar surface density, and $\gamma = 0.5$ for $\Sigma_{\rm total} > 100\ M_\odot\ {\rm pc}^{-2}$ and 0 otherwise. We use an iterative approach to determine $\alpha_{\rm CO}$ for each beam-sized line-of-sight region by (i) calculating the initial gas surface density with $\alpha_{\rm CO} = 4.35\ M_\odot\ ({\rm K\ km\ s^{-1}\ pc^2})^{-1}$, (ii) deriving $\alpha_{\rm CO}$ based on Equation (4), (iii) recalculating the gas surface density with the updated $\alpha_{\rm CO}$, and (iv) repeating this process until $\alpha_{\rm CO}$ changes by less than 0.1%.

3.3. Star Formation Rate Surface Density

To obtain SFR surface densities, we use the HST Hα observations matched to the resolution and pixel scale of the CO data. We measure the Hα flux along each beam-sized line-of-sight aperture in our two grids. We convert these fluxes to units of erg s^{-1} cm^{-2} Å^{-1} and apply a correction for extinction (see L. Lenkić et al. 2023, for details). Finally, we calculate Hα luminosities and convert them to SFRs using the relation of C.-N. Hao et al. (2011):

$${\rm SFR}[M_\odot\ {\rm yr}^{-1}] = 5.53 \times 10^{-42} \times L_{\rm H\alpha}[{\rm erg\ s^{-1}}]. \quad (5)$$

The global $\Sigma_{\rm SFR}$ values shown in Table 1 are from D. B. Fisher et al. (2019), and are derived from their global SFR and $R_{1/2}$ measurements (see their Tables 1 and 2).

3.4. Velocity Dispersion

To test theories of star formation, we finally must derive molecular gas velocity dispersions, which are considered to trace turbulence in the ISM. The ALMA CO observations allow us to measure the molecular gas velocity dispersion on 1–2 kpc scales and to compare these as a function of molecular gas and SFR surface densities to model predictions, which we will show in Section 4.4. Here, we outline our method for measuring molecular gas velocity dispersions and correcting for beam smearing.

To measure the velocity dispersion, we use the CO(3−2) observations when available, and the CO(4−3) observations otherwise. We begin by creating two overlapping grids of beam-sized apertures as described in Section 3. For each aperture, we then extract the spectrum of the CO line from the central pixel. We fit the line profile with a Gaussian function of the form $f(x) = a \times e^{(x-\mu_o)^2/2\sigma^2}$, where a is the amplitude of the line, μ_o is its centroid, and σ is its velocity dispersion. We perform our fitting using the PYTHON SCIPY function `curve_fit`. The resulting σ parameters obtained in this way are our velocity dispersion measurements.

However, beam smearing has a strong effect on measured velocity dispersion, particularly close to the centers of galaxies and along their minor axes. The effect of beam smearing can be significant even into the disk of the galaxies if their rotation curves rise slowly (G. Y. C. Leung et al. 2018). As a result, we apply a beam smearing correction to our measured velocity dispersions using the method of subtracting in quadrature an estimated value of the velocity dispersion due to beam smearing alone. We follow the procedure outlined in R. C. Levy et al. (2018), which we summarize here for completeness. To determine this correction, we first create model data cubes with no intrinsic dispersion. To accomplish this, we adopt the arctan model and rotation curve parameters from M. Girard et al. (2021) to calculate the rotation velocity ($v_{\rm rot}$) as a function of distance from the galaxy center (r):

$$v_{\rm rot}(r) = \frac{2}{\pi} \times V_{\rm rot} \times \arctan\left(\frac{r}{r_t}\right) \quad (6)$$

where $V_{\rm rot}$ is the rotation velocity in the flat region of the rotation curve and r_t is the "turnover radius" where the rotation curve transitions from rising to flat. We then calculate the observed velocity (i.e., in the plane of the sky; $v_{\rm obs}$) from

$$v_{\rm obs}(x, y) = v_{\rm rot}(r) \times \sin(i) \times \cos(\theta) \quad (7)$$

where i is the inclination (from M. Girard et al. 2021) and $\cos(\theta)$ is defined as

$$\cos(\theta) = \frac{-(x - x_o) \times \sin(\phi) - (y - y_o) \times \cos(\phi)}{r \times \cos(i)} \quad (8)$$

where x_o and y_o are the coordinates of the galaxy center and ϕ is the galaxy position angle (see, e.g., K. G. Begeman 1989). Finally, r is defined in the plane of the galaxy as

$$r = \sqrt{\frac{(x - x_o)^2 + (y - y_o)^2}{\cos(i)^2}}. \quad (9)$$

We build our model cubes by creating an array of zeros with the same dimensions as the actual observed cube, and then calculating $v_{\rm obs}$ at each pixel using Equation (7). We match the resulting observed velocity to the closest channel and place a "line" (a delta function with a linewidth equal to one channel) in the model cube array at the corresponding pixel and channel. The amplitude of the line is equal to the brightness of the same pixel in the same channel of the observed data cube (in Jy beam^{-1}). After performing this for each pixel, we smooth the cube with a Gaussian whose FWHM matches the resolution of the observation. Then, we fit the model CO line profile with a Gaussian, as above, to estimate the velocity dispersion due to beam smearing. Finally, we apply the beam smearing correction by subtracting the model velocity dispersion ($\sigma_{\rm CO,model}$) from the observed velocity dispersion ($\sigma_{\rm CO,observed}$) in quadrature for each beam-sized line-of-sight aperture to obtain the final beam-smearing-corrected velocity dispersion ($\sigma_{\rm CO,corrected}$) measurements.

In Figure 1, we show the steps of this correction for DYNAMO G04-1. In the top panels of Figure 1, we show the observed (left panel) and modeled (middle panel) moment 1 maps of DYNAMO G14-1, and the residuals ($v_{\rm obs} - v_{\rm mod}$) in

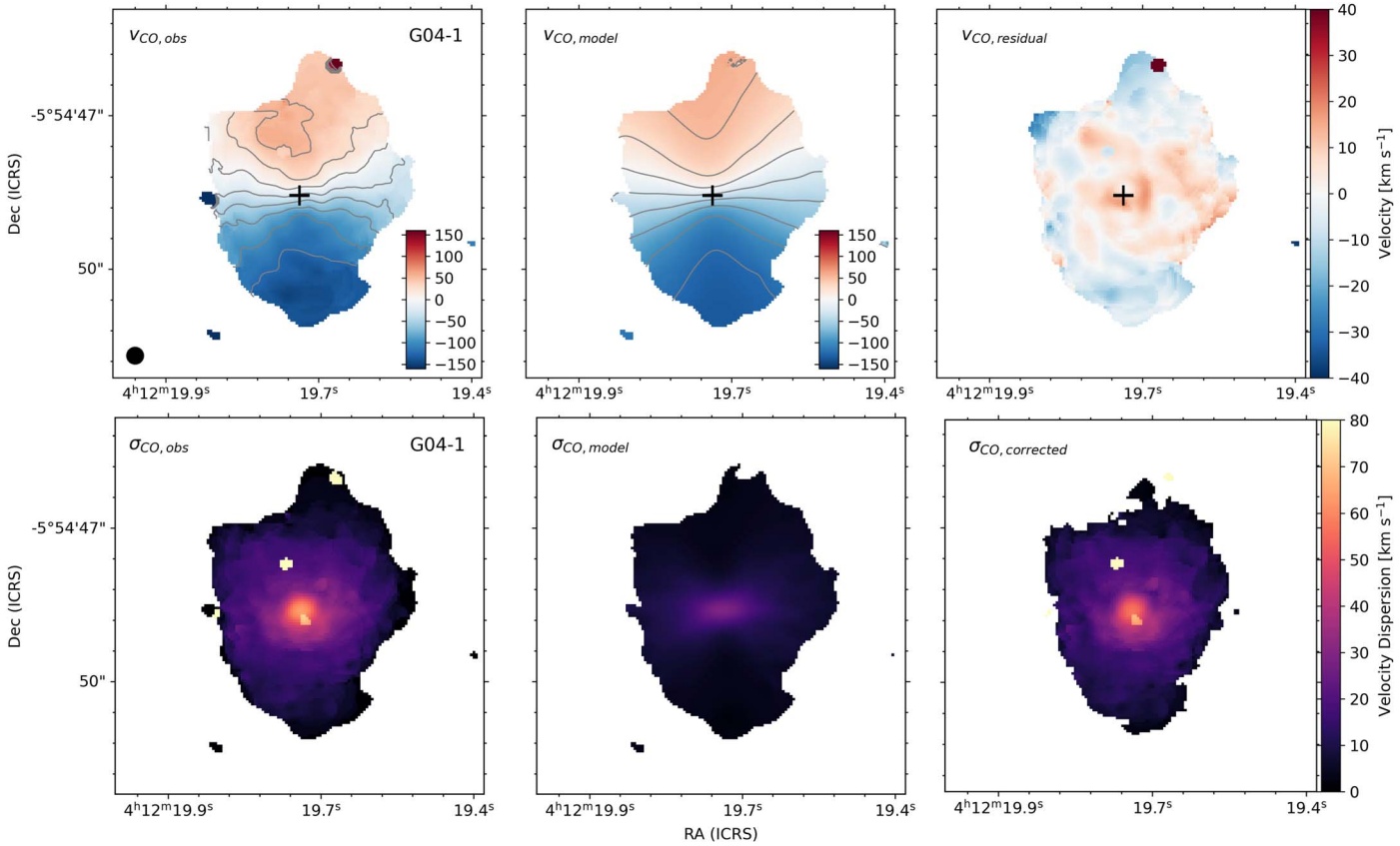

Figure 1. Observed and modeled velocity field and velocity dispersion maps of DYNAMO G04-1. Left: the observed velocity field (top) and velocity dispersion (bottom). Middle: the modeled velocity field (top) and velocity dispersion (bottom), derived from a model data cube. Right: the velocity field residuals we obtain by subtracting the model velocity field from the observations (top), and the corrected velocity dispersion map obtained by subtracting in quadrature the model velocity dispersion from our measured velocity dispersion. This simulates the effect of beam smearing and corrects for it.

the rightmost panel. The residuals for DYNAMO G04-1 show a pattern of positive residuals that resemble the spiral arms of this galaxy. The bottom panels of Figure 1 show the observed (left panel) and modeled (middle panel) velocity dispersions, while the rightmost panel shows the observed velocity dispersion map after beam smearing correction ($\sqrt{\sigma^2_{\rm obs} - \sigma^2_{\rm mod}}$).

The global $\sigma_{\rm mol}$ values we report in Table 1 are from M. Girard et al. (2021). The authors model the ALMA CO data cubes with GalPak^{3D} (N. Bouché et al. 2015). The cubes are fit directly with an arctan function, and velocity dispersion is assumed to be constant across the disk. The model is then convolved with the beam and line-spread function, which accounts for beam smearing.

4. Results

Our sample consists of nearly 500 kiloparsec-scale measurements of the star-forming, stellar, and gas masses, and the velocity dispersion properties across seven DYNAMO galaxies. Because DYNAMO galaxies resemble $z \sim 1$ star-forming systems, we can now investigate the relationships between these quantities and what they reveal about star formation regulation at physical scales not yet achievable in the high-redshift Universe.

4.1. Galaxy-averaged Relationship between σ_{mol}, σ_{ion}, and Σ_{SFR}

In Figure 2, we compare the velocity dispersion and $\Sigma_{\rm SFR}$ of DYNAMO galaxies to those of several other samples, spanning a range of systems from local spirals to $z \sim 5$ galaxies. We show comparisons to both ionized gas (right panel) and molecular gas (left panel).

Several studies have discussed the similarities of ionized gas velocity dispersions of DYNAMO galaxies to those of $z \sim 1$ galaxies (A. W. Green et al. 2014; R. Bassett et al. 2014; P. Oliva-Altamirano et al. 2018). In Figure 2, we reiterate this result. D. B. Fisher et al. (2019) compiled a list of high-quality ionized gas velocity dispersion measurements for DYNAMO galaxies using data from Gemini/GMOS and Keck/OSIRIS. The average $\sigma_{\rm ion}$ from that sample of 17 galaxies is 47 km s^{-1}. The galaxy-averaged velocity dispersions and $\Sigma_{\rm SFR}$ of DYNAMO galaxies are most similar to those of galaxies from the MASSIV sample ($z \sim 1$; B. Epinat et al. 2012), where the average $\sigma_{\rm ion}$ is 53 km s^{-1}. In comparison to $z \sim 0$ galaxies from the SAMI survey (M. R. Varidel et al. 2020), the DYNAMO velocity dispersions are over twice as high as the average of the SAMI sample, where $\sigma_{\rm ion} \sim 20$ km s^{-1}.

There are significantly fewer measurements of molecular gas velocity dispersion for comparison; nevertheless, for the data that exist in the literature we find a similar result. M. Girard et al. (2021) find that the average $\sigma_{\rm mol}$ for DYNAMO galaxies is $\sim$13 km s^{-1}. In contrast, the average $\sigma_{\rm mol}$ for galaxies in the PHANGS sample is $\sim$7 km s^{-1}. Because the inclination can increase the measured velocity dispersion, this average corresponds to PHANGS galaxies with inclinations $<50°$, which is similar to our DYNAMO sample. For comparison to $z \sim 1$–2 galaxies, we combine the samples of H. Übler et al. (2019) and M. Girard et al. (2019), noting the caveat that this

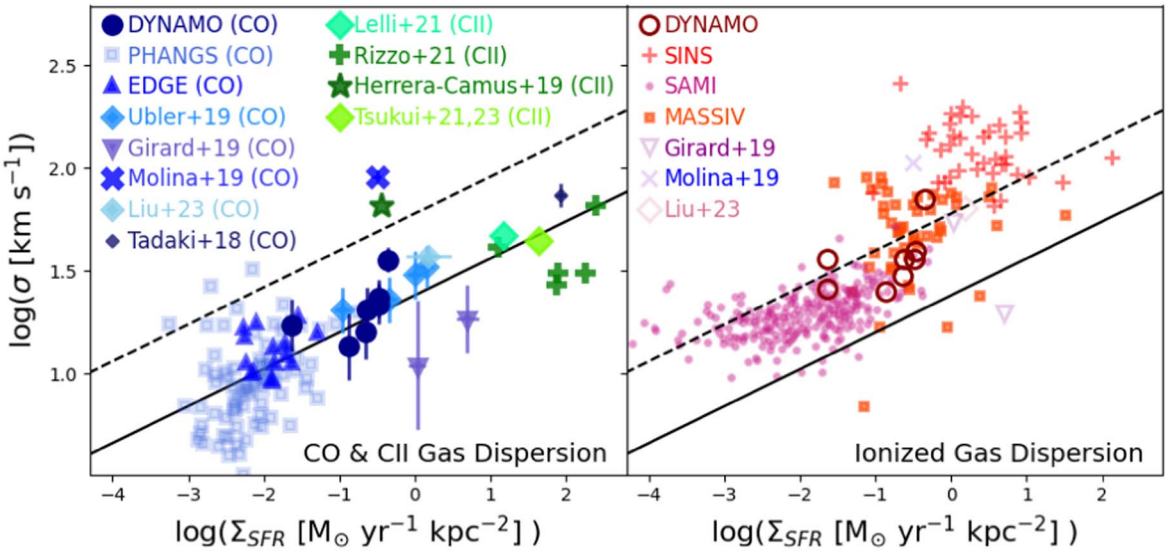

Figure 2. Global values of velocity dispersion, using the median dispersion from the moment maps, and $\Sigma_{\rm SFR}$ are compared to several samples for both cold gas tracers (CO and [C II]) on the left and ionized gas on the right. There is a significant correlation between $\Sigma_{\rm SFR}$ and velocity dispersion, with a systematic offset to higher dispersion when measured with ions. In both panels, the solid line indicates a fit to $\Sigma_{\rm SFR}$ and $\sigma_{\rm mol}$, and the dashed line represents $2.5 \times \sigma_{\rm mol}$. CO data from literature sources are taken from PHANGS ($z \sim 0$; J. Sun et al. 2023), EDGE ($z = 0.005-0.03$; R. C. Levy et al. 2018), H. Übler et al. (2019; $z \sim 2$), M. Girard et al. (2019; $z \sim 1$–1.5), J. Molina et al. (2019; $z \sim 1.5$), D. Liu et al. (2023; $z \sim 2$), K. Tadaki et al. (2018; $z \sim 4$); for [C II] they are taken from F. Lelli et al. (2021; $z \sim 5$), F. Rizzo et al. (2021; $z \sim 4-5$), R. Herrera-Camus et al. (2022; $z \sim 5.5$), T. Tsukui & S. Iguchi (2021), and T. Tsukui et al. (2023; $z \sim 4.4$). Ionized gas velocity dispersion measurements are taken from SAMI ($z \sim 0$; M. R. Varidel et al. 2020), MASSIV ($z \sim 1$–1.5; B. Epinat et al. 2012), and SINS ($z \sim 2$; N. M. Förster Schreiber et al. 2011).

results in a sample of only six heterogeneously selected galaxies. The typical $\sigma_{\rm mol}$ for this sample of six $z \sim 1$ targets is $\sim$20 km s^{-1}.

In Figure 2, we also show a fitted curve between $\sigma_{\rm mol}$ and $\Sigma_{\rm SFR}$ for the full sample of galaxies in the literature (we have weighted the PHANGS galaxies down by a factor of five, so that they do not dominate the minimization). The sources of comparison include: CO observations of $z = 0$ galaxies from the PHANGS (J. Sun et al. 2023) and EDGE (R. C. Levy et al. 2018) samples; CO observations of $z \sim 1$–2 galaxies from PHIBBS (H. Übler et al. 2019), three lensed galaxies (M. Girard et al. 2019; D. Liu et al. 2023), and a single target from the SHiZELS sample (J. Molina et al. 2019). At higher redshift, the only target with CO velocity dispersion measurements is AzTEC-1 (K. Tadaki et al. 2018); therefore, we also add galaxies in which the velocity dispersion is traced by [C II] (F. Lelli et al. 2021; F. Rizzo et al. 2021; R. Herrera-Camus et al. 2022). We offer the strong caveat that the sample is not homogeneously selected and there is a difference in data quality from the low-z targets of DYNAMO, PHANGS, and EDGE to the high-z targets. Nevertheless, without large ALMA programs, this is the only means to derive such correlations.

We find a correlation between the galaxy-averaged molecular gas velocity dispersion and $\Sigma_{\rm SFR}$, such that

$$\log \sigma_{\rm mol} = (0.19 \pm 0.03) \times \log \Sigma_{\rm SFR} + (1.33 \pm 0.04). \quad (10)$$

In both panels of Figure 2, we also show a dashed line that represents $2.5 \times \sigma_{\rm mol}$. This is the scale factor that was found by M. Girard et al. (2021) from the fitted relationship between $\sigma_{\rm mol}$ and $\sigma_{\rm ion}$, which appears to show overall agreement with the data here. We note that there are two very high $\sigma_{\rm mol}$ outliers to this power law: they are SHiZELS-19 (J. Molina et al. 2019) and HZ4 (R. Herrera-Camus et al. 2022). Given the small number of targets at high $\Sigma_{\rm SFR}$, we are careful not to merely dismiss these as they may represent an important subset of galaxies at high z or point to differences in analysis techniques. More data are clearly needed to study this important power law for galaxy properties.

The power law that we find in Figure 2 is very similar to the power law found in the recent SILCC simulations (T.-E. Rathjen et al. 2023). The authors run a set of simulations with varying $\Sigma_{\rm mol}$ that incorporate feedback to drive the velocity dispersions. A similar fit between $\sigma_{\rm mol}$ and $\Sigma_{\rm SFR}$ yields a slope of 0.2. They find a constant offset between the warm (ionized) and cold (molecular) gas velocity dispersions of $\sim$2.2. We note that the SILCC simulations do not incorporate large-scale instabilities that are often invoked to explain large velocity dispersion, but rather drive the velocity dispersion only through a complex model of star formation feedback. In this model they can recover the velocity dispersions of both the ions and the molecular gas.

4.2. Σ_{mol}–Σ_* Relation

In Figure 3, we show the relationship between $\Sigma_{\rm mol}$ and Σ_*. DYNAMO measurements are presented as blue circles, while the black squares correspond to measurements from the PHANGS–ALMA survey (J. Sun et al. 2020; A. K. Leroy et al. 2021), which have been smoothed to kiloparsec-scale resolution to match our observations. PHANGS–ALMA observed 90 nearby ($d \lesssim 20$ Mpc) galaxies that are on or near the $z = 0$ main sequence in CO(2−1) at $\sim$100 pc resolution, and J. Sun et al. (2020) present results for 70 of these targets, consisting of 102,778 independent lines of sight. The data we show in Figure 3 and subsequent ones include only lines of sight from galaxies with inclinations less than 50° (corresponding to the largest inclination in our sample). The $\Sigma_{\rm mol}$–Σ_* relationship is sometimes referred to as the "molecular gas

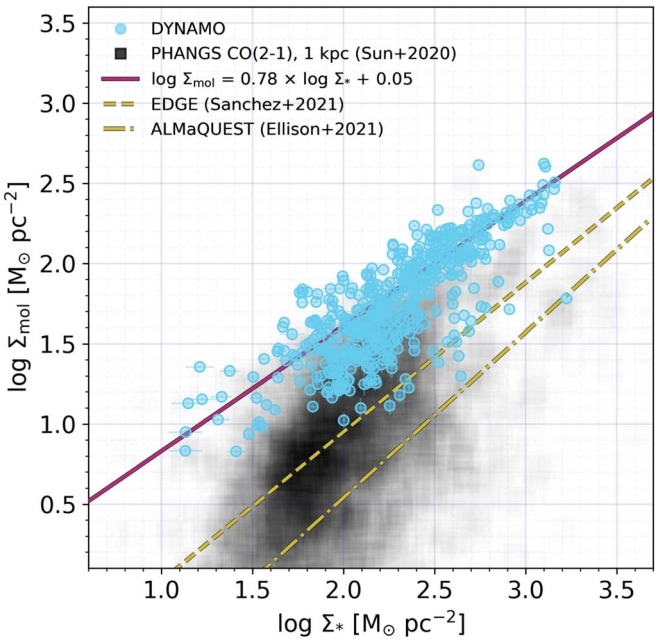

Figure 3. The molecular gas mass surface density as a function of stellar mass surface density. The blue data points correspond to DYNAMO ∼1–2 kpc line-of-sight measurements, assuming a variable α_{CO} conversion factor as described by Equation (4). For comparison, we include the PHANGS CO(2−1) ∼1 kpc line-of-sight measurements as black data points, and best-fit lines from local galaxy samples in EDGE–CALIFA (yellow dashed line; J. K. Barrera-Ballesteros et al. 2020; S. F. Sánchez et al. 2021) and ALMaQUEST (yellow dashed–dotted line; S. L. Ellison et al. 2021a). We also perform an ODR fit to the DYNAMO measurements (solid purple line), which shows that DYNAMO galaxies are fitted by a shallower slope and larger normalization. DYNAMO galaxies are fundamentally more gas-rich than local spirals at all disk positions.

main sequence." It has been measured for several samples in nearby galaxies (L. Lin et al. 2019; J. K. Barrera-Ballesteros et al. 2020; S. L. Ellison et al. 2021b; S. F. Sánchez et al. 2021), and is often thought to drive the star formation main sequence, in combination with the KS relation (S. L. Ellison et al. 2021a; W. M. Baker et al. 2023), although other studies find no conclusive evidence for this (see, e.g., S. F. Sánchez et al. 2021). S. L. Ellison et al. (2021a) showed that of the correlations between Σ_{SFR}, Σ_*, and Σ_{mol}, the tightest relationship is between Σ_* and Σ_{mol}, with a scatter of ∼0.19 dex in their ALMaQUEST sample. Moreover, the scatter in the $\Sigma_*-\Sigma_{mol}$ relationship does not correlate to scatter in the KS relation. We can therefore use this as an independent means of comparing resolved Σ_{mol} in DYNAMO galaxies to that of local spirals. We note there are not a sufficient number of galaxies observed at $z > 1$ for a similar comparison.

We show in Figure 3 that an orthogonal distance regression (ODR) fit to the resolved regions in DYNAMO galaxies yields a sublinear relationship that is offset to higher Σ_{mol} than the relationships derived on local spirals (L. Lin et al. 2019; J. K. Barrera-Ballesteros et al. 2020; S. L. Ellison et al. 2021b; S. F. Sánchez et al. 2021). The relationship we determine for DYNAMO galaxies is

$$\log \Sigma_{mol} = (0.78 \pm 0.03) \times \log \Sigma_* + (0.05 \pm 0.07). \quad (11)$$

The extrapolation of this relationship toward low Σ_* does not project into the sequence of PHANGS galaxies. This brings up a useful insight into the nature of DYNAMO galaxies. They are not a continuation of the properties of spirals in the local Universe, nor are they in this way similar to the centers of local spirals. They are globally more gas-rich at all positions in the disk. DYNAMO galaxies have Σ_{mol}/Σ_* that is roughly an order of magnitude higher than local spirals at all values of Σ_* observed. This is consistent with previous global measurements of gas fractions in DYNAMO galaxies being higher than in galaxies in the local Universe (D. B. Fisher et al. 2014, 2019; H. A. White et al. 2017).

4.3. Resolved Molecular KS Relation at High Σ_{SFR}

We have shown that the DYNAMO galaxies in our sample are systematically more gas-rich than local star-forming galaxies; this allows us to derive the KS relation at kiloparsec scales for systems that are selected to resemble $z \sim 1$ galaxies, where such resolved observations are still challenging. This is what we present in Figure 4. The left panel assumes a constant Milky Way α_{CO} for deriving Σ_{mol}, while the right panel assumes a variable α_{CO} (see Section 3.2). Measurements of Σ_{mol} and Σ_{SFR} by J. Sun et al. (2020) from the PHANGS–ALMA CO(2−1) survey (A. K. Leroy et al. 2021), matched to the kiloparsec-scale resolution of our observations, are included as black squares.

We fit our measurements assuming both a constant and a variable α_{CO} with a power law of the form $\log \Sigma_{SFR} = N \times \log \Sigma_{mol} + C$ using ODR. In the case of constant α_{CO}, we find

$$\log \Sigma_{SFR} = (0.90 \pm 0.04) \times \log \Sigma_{mol} - (2.70 \pm 0.08) \quad (12)$$

when fitting the DYNAMO measurements alone (which is very similar to the slope of $N = 0.92$ from J. Sun et al. (2023), when assuming a Milky Way α_{CO}), and

$$\log \Sigma_{SFR} = (1.04 \pm 0.01) \times \log \Sigma_{mol} - (3.15 \pm 0.02) \quad (13)$$

when fitting the DYNAMO and PHANGS measurements together. In the case of variable α_{CO}, we find

$$\log \Sigma_{SFR} = (1.23 \pm 0.03) \times \log \Sigma_{mol} - (3.08 \pm 0.06) \quad (14)$$

for the DYNAMO data, which is very similar to the slope of $N = 1.21$ from J. Sun et al. (2023) when they assume the same prescription of variable α_{CO}.

The near-unity slopes we find in the case of constant Milky Way α_{CO} would suggest that the depletion time ($t_{dep} = \Sigma_{mol}/\Sigma_{SFR}$) in DYNAMO is roughly constant. The purple dotted lines in Figure 4 indicate constant depletion times of 0.1, 1, and 10 Gyr from top left to bottom right. We can see from this that more than half of the DYNAMO line-of-sight measurements (297/490) have $t_{dep} < 1$ Gyr. In fact, the median depletion time and 16th−84th percentile ranges we find are $t_{dep} = 0.8^{+0.9}_{-0.4}$ Gyr. This is significantly lower than J. Sun et al. (2023), who find a median $t_{dep} = 2.1^{+1.9}_{-1.1}$ Gyr when they assume a constant Milky Way α_{CO} in over 2000 kiloparsec-sized apertures across the full sample of 80 galaxies from PHANGS–ALMA.

When we adopt an α_{CO} that varies with local gas plus stellar mass surface density (A. D. Bolatto et al. 2013), we find a steeper slope of $N = 1.23$, suggesting that depletion time is not constant in DYNAMO and becomes shorter at higher Σ_{mol} and

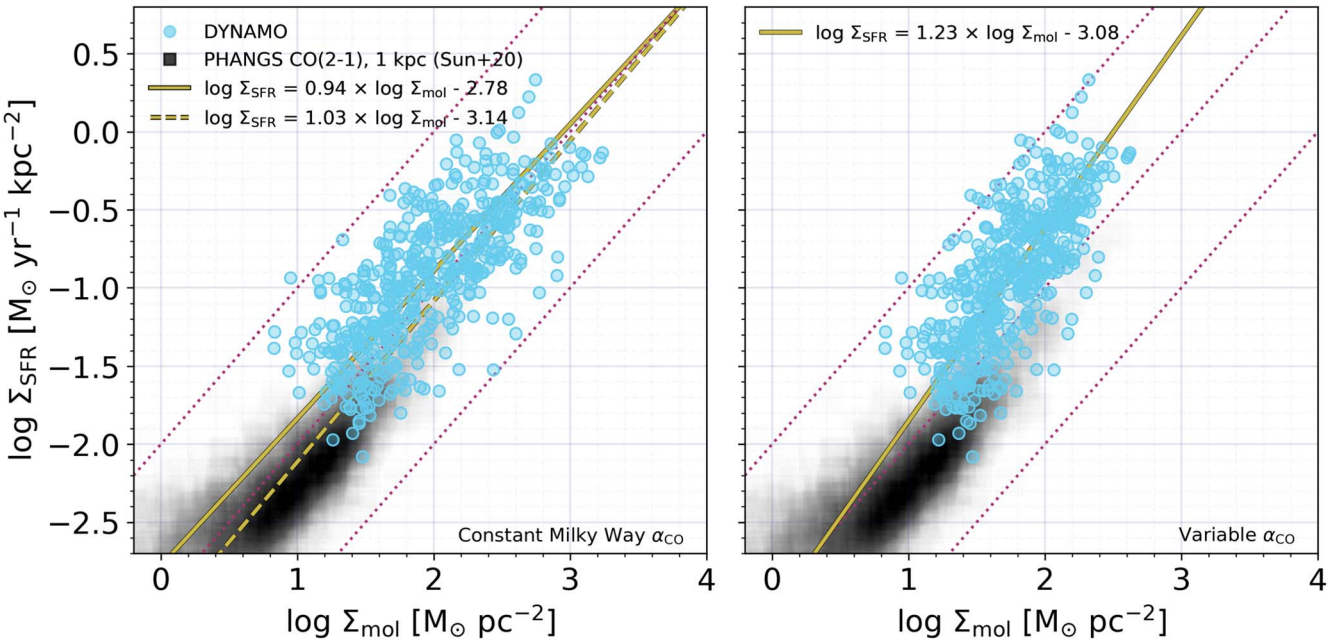

Figure 4. The kiloparsec-scale resolved Kennicutt–Schmidt relation for DYNAMO galaxies with $\Sigma_{\rm mol}$ measured assuming a constant $\alpha_{\rm CO}$ (left panel) and a varying $\alpha_{\rm CO}$ (right panel). We include the ∼1 kpc-scale measurements of J. Sun et al. (2020) for PHANGS galaxies, using CO(2−1) maps and SFRs derived from Hα + 24 μm, as black squares. The solid yellow line shown in both panels is the best-fit line (determined using orthogonal linear regression) to the DYNAMO measurements. The dashed yellow line is the best-fit relation to the DYNAMO and PHANGS data combined. The dotted purple lines indicate constant molecular gas depletion times of 0.1, 1, and 10 Gyr (from top left to bottom right).

$\Sigma_{\rm SFR}$. In this case, nearly all DYNAMO regions have depletion times shorter than 1 Gyr (415/490), and the median depletion time is $t_{\rm dep} = 0.5^{+0.5}_{-0.3}$ Gyr. Similarly, in a case study of the nearby ($z \sim 0.02$) high-redshift galaxy analog IRAS 08339 +6517, D. B. Fisher et al. (2022) find a variation in depletion time by two orders of magnitude with $t_{\rm dep} < 0.1$ Gyr in the central kiloparsec and $t_{\rm dep} > 3$ Gyr at radii greater than ∼2.5 kpc. Conversely, J. Sun et al. (2023) find a median $t_{\rm dep} = 1.9^{+1.5}_{-1.0}$ Gyr when assuming the prescription of variable $\alpha_{\rm CO}$ of A. D. Bolatto et al. (2013).

In addition to PHANGS–ALMA, there are several additional surveys of local galaxies that have measured the molecular KS relation on kiloparsec scales that we can compare to. S. L. Ellison et al. (2021a) use 15,000 kiloparsec-sized spaxels across 28 galaxies ($0.02 < z < 0.05$) from ALMaQUEST to find a slope of $N = 1.23 \pm 0.01$ when assuming a Milky Way $\alpha_{\rm CO}$. This is higher than our slope of $N = 0.94$ under the same assumption for $\alpha_{\rm CO}$. For comparison, the authors also assume the prescription of metallicity-dependent $\alpha_{\rm CO}$ of J. Sun et al. (2023) and find a slope of $N = 1.27$. J. Sun et al. (2023) show that the prescription of variable $\alpha_{\rm CO}$ of A. D. Bolatto et al. (2013) leads to a higher slope than their fiducial metallicity-dependent $\alpha_{\rm CO}$. In contrast, S. F. Sánchez et al. (2021) find a slope of 0.98 ± 0.14 for ∼15,500 kiloparsec-scale line-of-sight measurements from EDGE–CALIFA for a constant Milky Way CO-to-H_2 conversion factor. For ∼14,500 kiloparsec-scale measurements across a sample of 30 nearby disk galaxies from HERACLES (A. K. Leroy et al. 2009), A. K. Leroy et al. (2013) find a slope of $N = 1.00 \pm 0.15$ for the KS relation when assuming a Milky Way $\alpha_{\rm CO}$, consistent with our results. However, they find that the median gas depletion time is 2.2 Gyr with 0.3 dex scatter, consistent with the PHANGS–ALMA results but longer than our depletion time of $t_{\rm dep} = 0.8^{+0.9}_{-0.4}$ Gyr when assuming a constant Milky Way $\alpha_{\rm CO}$.

4.4. Resolved Correlations of σ_{mol}–Σ_{mol}, σ_{mol}–Σ_{SFR}, and σ_{mol}–t_{dep}

Figure 5 presents the $\sigma_{\rm mol}$–$\Sigma_{\rm mol}$ relation in the left panel, and the $\sigma_{\rm mol}$–$\Sigma_{\rm SFR}$ relation in the right panel, where all measurements are made along ∼1–2 kpc-sized apertures. As in previous figures, DYNAMO data points are in blue while the kiloparsec-scale matched-resolution measurements of $\sigma_{\rm mol}$, $\Sigma_{\rm mol}$, and $\Sigma_{\rm SFR}$ by J. Sun et al. (2020) from PHANGS–ALMA are included as black squares. In both panels, the solid yellow line is an ODR power-law fit to both the DYNAMO and PHANGS measurements:

$$\log \sigma_{\rm mol} = (0.48 \pm 0.02) \times \log \Sigma_{\rm mol} + (0.47 \pm 0.03) \quad (15)$$

and

$$\log \sigma_{\rm mol} = (0.27 \pm 0.2) \times \log \Sigma_{\rm SFR} + (1.56 \pm 0.02). \quad (16)$$

We make several observations from Figure 5. First, we note that the results of our $\sigma_{\rm mol}$–$\Sigma_{\rm mol}$ relation are consistent with the kiloparsec-scale measurements of J. Sun et al. (2020): regions of more active star formation tend to host molecular gas with higher surface densities. J. Sun et al. (2020) compare the centers of barred galaxies to disk regions and find that barred centers have ∼20× higher mass-weighted molecular gas surface densities and 5× higher mass-weighted median molecular gas velocity dispersions. The authors attribute these high $\Sigma_{\rm mol}$ and $\sigma_{\rm mol}$ values to the presence of stellar bars, which drive large-scale gas inflows, boosting $\Sigma_{\rm mol}$, and enhance local turbulence through the release of gravitational potential energy.

We also see in the left panel of Figure 5 that despite being local galaxies, DYNAMO systems are unlike the PHANGS–ALMA nearby targets, because DYNAMO galaxies have high $\sigma_{\rm mol}$ and $\Sigma_{\rm mol}$ everywhere in their disks (though the centers of

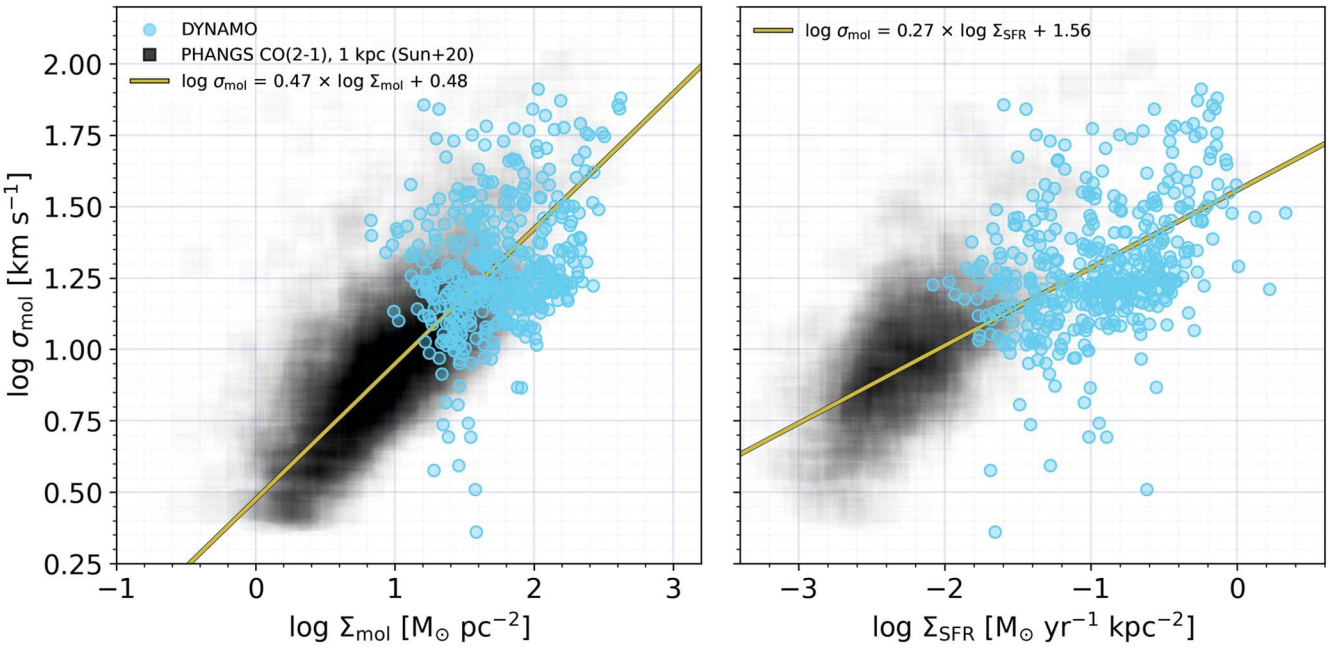

Figure 5. Beam-smearing-corrected molecular gas velocity dispersions as a function of molecular gas surface density (left) and star formation rate surface density (right), for individual ∼1–2 kpc-scale line-of-sight measurements in seven DYNAMO galaxies. The black squares correspond to the PHANGS–ALMA derived measurements of J. Sun et al. (2020) in 70 nearby galaxies, at a resolution of 1 kpc to match our observations (J. Sun 2024, private communication). Consistent with the PHANGS–ALMA results, velocity dispersions in DYNAMO galaxies increase with $\Sigma_{\rm mol}$ and $\Sigma_{\rm SFR}$. In contrast to PHANGS, DYNAMO galaxies populate the regime of high $\sigma_{\rm mol}$, $\Sigma_{\rm mol}$, and $\Sigma_{\rm SFR}$ of this parameter space. Furthermore, these high values are observed throughout the entire disks of DYNAMO galaxies, not just their central regions.

DYNAMO galaxies do also exhibit higher $\sigma_{\rm mol}$; see Figure A3). The DYNAMO galaxies we study are not barred in near-IR starlight images. However, they have been shown to have low values of Toomre Q, indicating galaxy-wide instabilities (D. B. Fisher et al. 2017a; H. A. White et al. 2017). Such instabilities are likewise associated to inflows in disks (A. Dekel & A. Burkert 2014), which are seen in the nearby clumpy, blue compact disk galaxy IRAS 08339+6517 (D. B. Fisher et al. 2022).

In Figure 6, we plot the molecular gas velocity dispersion as a function of depletion time, assuming a variable $\alpha_{\rm CO}$. We find an inverse relation between these two quantities, as was found by D. B. Fisher et al. (2019) for galaxy-averaged values of $\sigma_{\rm mol}$ and $t_{\rm dep}$ for a sample of 14 galaxies, including 10 DYNAMO galaxies. The authors found that $\sigma_{\rm mol} \propto t_{\rm dep}^{-0.72}$, while the best fit to our kiloparsec-scale resolved DYNAMO measurements combined with PHANGS is

$$\log \sigma_{\rm mol} = (-0.80 \pm 0.07) \times \log t_{\rm dep} + (1.00 \pm 0.03). \quad (17)$$

Feedback-regulated models of star formation (see, e.g., E. C. Ostriker & R. Shetty 2011; R. Shetty & E. C. Ostriker 2012; C.-A. Faucher-Giguere et al. 2013), where the gravitational force of the gas in the disk balances the momentum-flux injected into the ISM by supernovae, predict that velocity dispersion is linearly inversely proportional to the depletion time, i.e., $\sigma_{\rm mol} \propto t_{\rm dep}^{-1}$.

C.-A. Faucher-Giguere et al. (2013) argue that the important timescale for turbulence to dissipate within the disk is the vertical crossing time related to the disk thickness and is proportional to the orbital time for Q~1. We combine Equations (6) and (18) of C.-A. Faucher-Giguere et al. (2013) to predict that

$$\sigma \propto \frac{P_*}{m_*} \times \frac{\Sigma_{\rm SFR}}{\Omega\, \Sigma_{\rm gas}} = \frac{P_*}{m_*} \times \frac{t_{\rm orb}}{t_{\rm dep}}. \quad (18)$$

where $\Omega = v_c/r$ is the angular frequency, $t_{\rm orb} = \Omega^{-1}$ is the orbital time, and P_*/m_* is the momentum returned to the ISM by stellar feedback per stellar mass formed. If we assume $P_*/m_* = 3000\ {\rm km\ s^{-1}}$ and adopt our measured values of $\Sigma_{\rm SFR}$, $\Sigma_{\rm mol}$, and Ω, then we are able to calculate the values of $\sigma_{\rm mol}$ that would be predicted by this simple feedback-regulated star formation model, and compare to our observed $\sigma_{\rm mol}-\Sigma_{\rm SFR}$ and $\sigma_{\rm mol}-\Sigma_{\rm mol}$ relations.

Taking the dynamical models of M. Girard et al. (2021), it is straightforward to determine that $t_{\rm orb}$ is shortest in the galaxy center, where we find both $\Sigma_{\rm mol}$ and $\sigma_{\rm mol}$ to be largest. This exercise reveals that the $\sigma_{\rm mol}$ values predicted by Equation (18) decrease with increasing $\Sigma_{\rm mol}$ and $\Sigma_{\rm SFR}$, which is opposite to the behavior we observe in Figure 5. The $\sigma_{\rm mol} \propto t_{\rm dep}^{-1}$ dependence in Equation (18) is order-of-magnitude compatible with our $\sigma_{\rm mol} \propto t_{\rm dep}^{-0.8}$ dependence; therefore, we suggest that the assumption that turbulent momentum decay takes place on an eddy (disk) crossing time and is proportional to Ω is incompatible with our observations and is the cause of the discrepancy between the predicted $\sigma_{\rm mol}$ and our observed values.

5. Discussion

5.1. Comparison of $\sigma_{mol}-\Sigma_{SFR}$ and $\sigma_{mol}-\Sigma_{mol}$ to Hydrodynamic Models and Theory

In this section, we further explore our $\sigma_{\rm mol}-\Sigma_{\rm SFR}$ relation within the context of theories of star formation regulation by

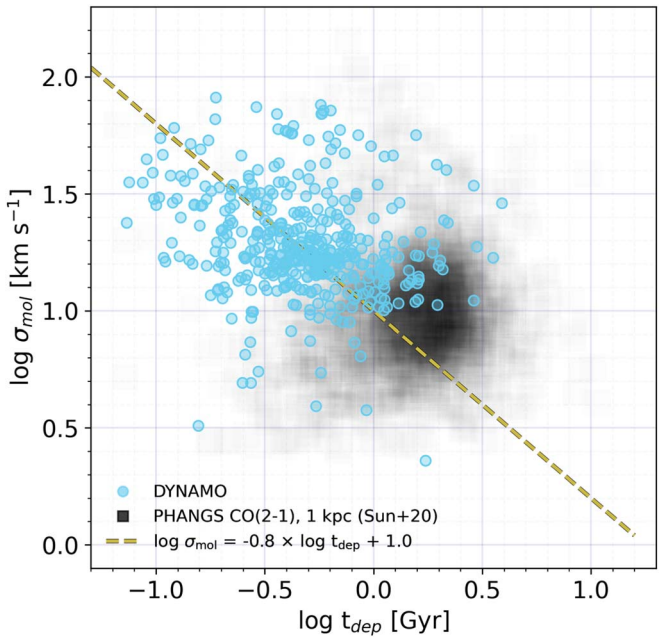

Figure 6. Beam-smearing-corrected molecular gas velocity dispersion as a function of the gas depletion time ($t_{\rm dep}$), measured along individual ∼1–2 kpc-sized lines of sight and assuming a variable $\alpha_{\rm CO}$. Compared to PHANGS, DYNAMO disks have overall shorter depletion times. As we would expect, the shorter depletion times are at smaller galactocentric radii, where the velocity dispersions are greater. The yellow dashed line represents the best fit to the DYNAMO+PHANGS measurements.

comparing our observed relations to predictions from theory and results from numerical simulations.

5.1.1. Gravitational and Stellar Feedback-driven Turbulence

In the left panel of Figure 7, we first compare the DYNAMO and PHANGS–ALMA results to the predictions of M. R. Krumholz et al. (2018). They develop a model where the sources of turbulence in galaxy disks include both feedback from star formation and the release of gravitational potential energy from gas inflows (see also K. Wada et al. 2002; F. Bournaud et al. 2010; P. F. Hopkins & E. Quataert 2011). The relationship they derive between $\Sigma_{\rm SFR}$ and gas velocity dispersion (σ_g) is given by their Equation (59), which assumes MKS units:

$$\Sigma_{\rm SFR} = f_{\rm sf}\frac{\sqrt{8(1+\beta)}\,f_{g,Q}}{GQ}\frac{\sigma_{\rm g}}{t_{\rm orb}^2} \times \max\left[\frac{8\epsilon_{\rm ff}\,f_{g,Q}}{Q}\sqrt{\frac{2(1+\beta)}{3f_{g,P}\,\phi_{\rm mp}}}, \frac{t_{\rm orb}}{t_{\rm sf,max}}\right]. \quad (19)$$

In this equation, $f_{\rm sf} = [1.0, 0.5]$ is the fraction of the ISM in the molecular phase, $f_{g,Q} = [0.7, 0.5]$ is the fractional contribution of gas to Q, $t_{\rm orb} = [200, 200]$ Myr is the galaxy orbital time, and $f_{g,P} = [0.7, 0.5]$ is the fractional contribution of the gas self-gravity to the midplane pressure; these values are for high-redshift and local spiral galaxies respectively. The remaining parameters are the same for both high-redshift galaxies and local spirals: $\beta = 0$ is the rotation curve index, G is the gravitational constant, $Q = 1$ is the Q stability parameter (A. B. Romeo & N. Falstad 2013), $\epsilon_{\rm ff} = 0.015$ is the star-forming efficiency per freefall time, $\phi_{\rm mp} = 1.4$ is the ratio of total pressure to turbulent pressure at the midplane, and $t_{\rm sf,max} = 2$ Gyr is the maximum star-forming timescale. The values we quote here are the fiducial values adopted by M. R. Krumholz et al. (2018, see their Tables 1 and 3); using these values and converting to MKS units, we derive the following expression for the $\sigma_{\rm mol}$–$\Sigma_{\rm SFR}$ relation:

$$\sigma_{\rm mol,high-z} = \frac{1}{460 \times 0.977}\,t_{\rm orb}^2\,\Sigma_{\rm SFR} \times \max\left[\frac{8\epsilon_{\rm ff}\,f_{g,Q}}{Q}\sqrt{\frac{2(1+\beta)}{3f_{g,P}\,\phi_{\rm mp}}}, \frac{t_{\rm orb}}{t_{\rm sf,max}}\right]^{-1} \quad (20)$$

for high-redshift galaxies (yellow dashed curve in Figure 7), and

$$\sigma_{\rm mol,spiral} = 2.8 \times \sigma_{\rm mol,high-z} \quad (21)$$

for local spirals (yellow dotted curve in Figure 7). This framework predicts that the primary mechanism driving turbulence is a function of mass and redshift, with gravity-driven turbulence dominating in high-redshift galaxies and for high masses, and feedback-driven turbulence dominating at lower redshifts and masses. Furthermore, the model predicts that the maximum velocity dispersion that can be maintained by feedback alone is ∼6−10 km s^{-1}, where the exact value depends on the gas fraction, thermal velocity dispersion, and fraction of the ISM that is in the molecular hydrogen phase.

In the relevant properties for this theory (e.g., gas fraction, Q stability parameter; see Section 2.1), DYNAMO galaxies are most similar to those of $z \sim 1$ galaxies. There is evolution of properties such as $\Sigma_{\rm SFR}$ and the velocity dispersion from $z \sim 1$ to $z \sim 2$; therefore we expect that DYNAMO galaxies may fall between the "spiral" and "high-z" categories from M. R. Krumholz et al. (2018).

However, our comparison reveals that for the assumed fiducial parameters, both the local spiral and high-redshift curves overpredict the velocity dispersions that we observe in DYNAMO and those of PHANGS galaxies. This observation was also made by M. Girard et al. (2021) for global DYNAMO measurements of $\sigma_{\rm mol}$ and SFR (see their Figure 4) and by F. Roman-Oliveira et al. (2024) for a sample of four $z \sim 4.5$ galaxies (see their Figure 5).

The break in the model of Equation (20) can be shifted to higher or lower $\Sigma_{\rm SFR}$ values by revisiting the values we assume for the fiducial parameters: (1) decreasing the fraction of the ISM that is in the molecular phase, $f_{\rm sf}$, shifts the break in the model to smaller $\Sigma_{\rm SFR}$ values, which increases the discrepancy with the DYNAMO observations, (2) increasing the fractional contribution of the gas to Q, $f_{\rm g,Q}$, to 1 shifts the model break to only marginally higher $\Sigma_{\rm SFR}$, and (3) decreasing the orbital time, $t_{\rm orb}$, shifts the break to higher $\Sigma_{\rm SFR}$ values. To further explore this last option, we replicate the left panel of Figure 7 in Figure 8. First, we compute the rotation curve index, $\beta = d\ \ln(v)/d\ \ln(r)$, for each galaxy. We then determine the radius at which β deviates from a flat rotation curve ($\beta = 0$) by 25%. Because we are assuming $\beta = 0$ in Equation (19), for this comparison we exclude from Figure 8 any DYNAMO data points where the rotation curve is rising and $\beta \neq 0$. We now also color the DYNAMO data points according to the $t_{\rm orb}$ value at the corresponding radius ($t_{\rm orb} = 2\pi R/V$ and correcting for inclination). Where the rotation curves are flat, we see that the range of $t_{\rm orb}$ values for DYNAMO is ∼100–300 Myr. Thus, we now overplot the high-z (black dashed lines) and local spiral (black dotted lines) models of M. R. Krumholz et al. (2018) for

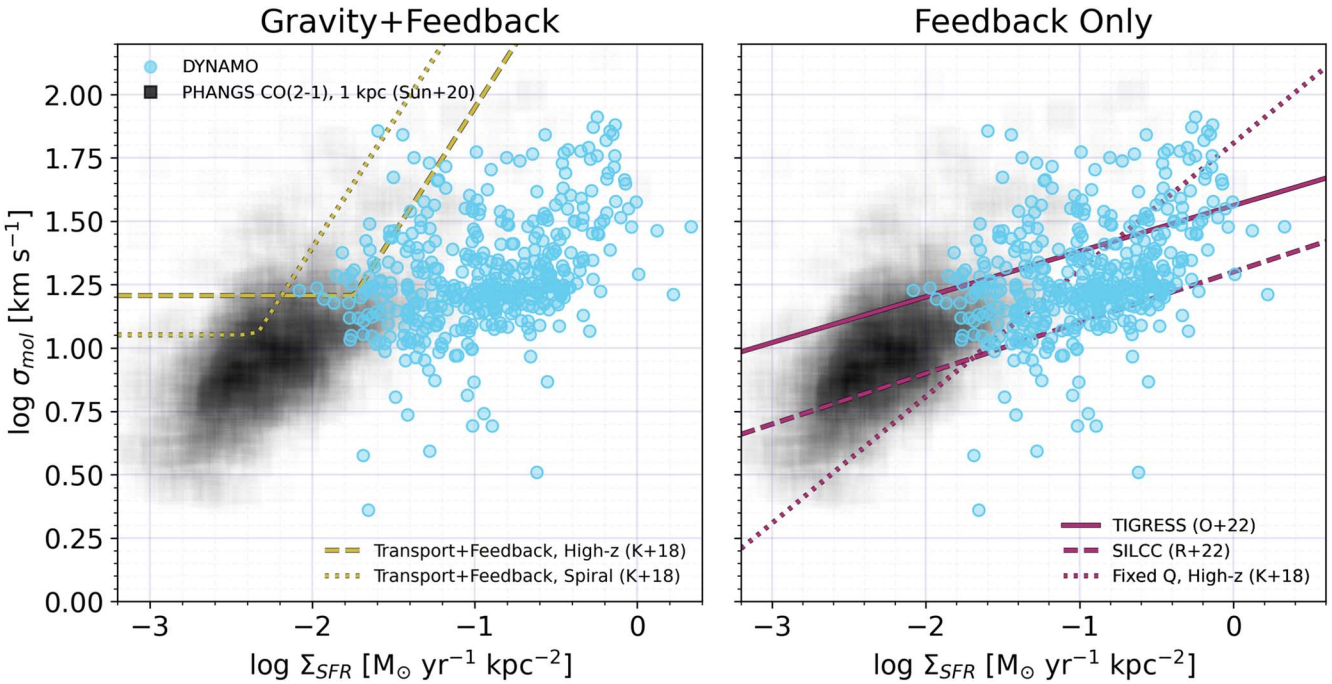

Figure 7. Left: comparison of DYNAMO (blue) and PHANGS (gray) $\sigma_{\rm mol}$ and $\Sigma_{\rm SFR}$ measurements to the prediction from the gas transport plus feedback model of M. R. Krumholz et al. (2018), where the yellow dashed line is the prediction for high-redshift galaxies and the yellow dotted line is for local spirals. This comparison shows that, for the fiducial parameters assumed by M. R. Krumholz et al. (2018), the transport+feedback models overpredict the DYNAMO and PHANGS velocity dispersions. Right: comparison of DYNAMO and PHANGS measurements to the results of the TIGRESS (solid purple line; E. C. Ostriker & C.-G. Kim 2022) and SILCC (dashed purple line; T.-E. Rathjen et al. 2023) simulations, which incorporate stellar feedback only, and the feedback-only model of M. R. Krumholz et al. (2018) assuming fixed Q and variable $\epsilon_{\rm ff}$ (dotted purple line).

$t_{\rm orb} = 300$, 200, and 100 Myr, from left to right. As DYNAMO galaxies are most similar to star-forming systems at $z \sim 1$, we expect the data points to fall somewhere between the high-z and local spiral lines. Instead, we find that the models overpredict the observed velocity dispersion measurements as the majority of the DYNAMO points fall to the right of the high-z, $t_{\rm orb} = 100$ Myr model. We note, however, that the general shape of the transport+feedback model provides a qualitative match to our observations.

Studies of global star-forming and molecular gas properties in high-redshift galaxies find similar results. F. Roman-Oliveira et al. (2024) compare global gas velocity dispersions from ALMA [C II] observations and SFRs inferred from measurements of total infrared luminosity for four $z \sim 4.5$ disks to the transport and feedback models of M. R. Krumholz et al. (2018). They find that for any assumption of maximum circular speed (M. R. Krumholz et al. 2018, see Equation (60)) of the galaxies, the transport models overpredict the observations (see their Figure 5, left panel) consistent with our results, while the feedback-only models (see their Figure 5, right panel) do not. F. Rizzo et al. (2024) find similar results for a sample of 57 $z = 0-5$ galaxies where cold gas tracers (CO, [C I], [C II]) are used to measure global velocity dispersions (see their Figure 4).

Observations show that galaxies must be continuously replenished with gas to maintain star formation on timescales longer than the typical 1–2 Gyr gas depletion times in local galaxies or the even shorter depletion times of high-redshift galaxies. Simulations show that cold, smooth streams of gas join the disks of high-redshift galaxies at large radii ($\sim$0.1–0.3 $\times$ the virial radius, or $\sim$10$\times$ the stellar scale length; M. Danovich et al. 2015), generating large gas surface densities in these outer regions (see also D. Kere et al. 2005; A. Dekel et al. 2009; C. W. Trapp et al. 2022). Motivated by this, O. Ginzburg et al. (2022) built upon the work of M. R. Krumholz et al. (2018) by including the conversion of accretion energy into turbulent energy as a third mechanism for driving turbulence in disks (see also B. G. Elmegreen & A. Burkert 2010; R. S. Klessen & P. Hennebelle 2010). They find that galaxies in dark matter halos that evolve to masses $\leqslant 10^{12}\ M_\odot$ by redshift $z = 0$ are dominated by feedback-driven turbulence. Galaxies in more massive halos are dominated by transport-driven turbulence or accretion-driven turbulence depending on the efficiency of converting accretion kinetic energy into turbulent energy. However, the effect of adding accretion-driven turbulence is to increase the floor in $\sigma_{\rm mol}$ that can be maintained by stellar feedback alone, which increases the discrepancy with our observations. It also decreases the level of star formation required to achieve very high velocity dispersions, which also increases the discrepancy with our observations (see Figure 6 in O. Ginzburg et al. 2022).

Finally, we compare our $\sigma_{\rm mol}-\Sigma_{\rm mol}$ relation to the work of N. Brucy et al. (2020), who conduct magnetohydrodynamic simulations of 1 kpc-sized cubic regions in local and high-z, gas-rich disks where the effects of stellar feedback (formation of H II regions, supernovae, and far-ultraviolet feedback) and turbulent forcing on large scales by an external force are considered independently and together. The authors find that stellar feedback alone is enough to suppress star formation to levels of the KS relation in nearby galaxies, but is insufficient to do so in high-z systems. For these, the authors argue that large-scale turbulent driving, from either mass accretion onto the galaxy, gas transport within the disk, or some other mechanism, is required (see also N. Brucy et al. 2023). They test two scalings for the turbulent driving: one where the mean power injected is $\overline{P_{\rm inj}} \propto \Sigma_{0,\rm gas}^{2.5}$, and a stronger form where

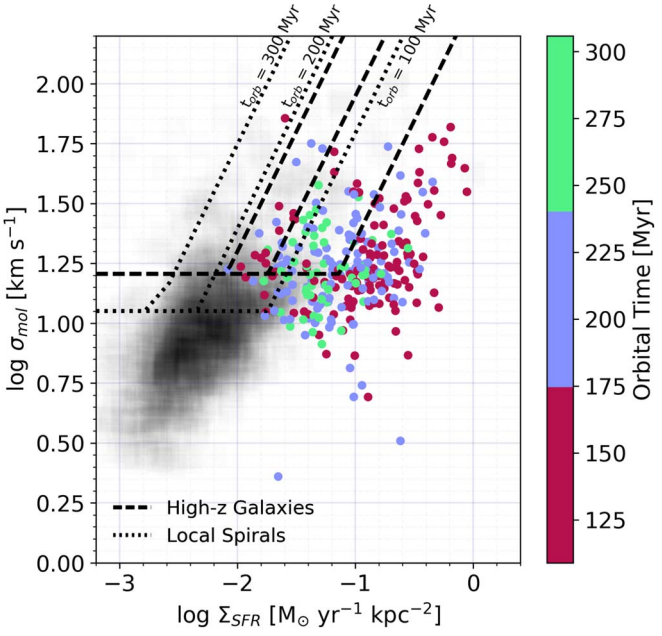

Figure 8. The same as the left panel of Figure 7; however, we now only include DYNAMO measurements at larger radii where the rotation curves are flat and the $\beta = 0$ assumption is valid. The range of t_{orb} for the DYNAMO points in this case is ∼100–300 Myr. The black dashed (dotted) lines are the models of M. R. Krumholz et al. (2018) for the high-z (local spiral) case, assuming $t_{orb} = 300$, 200, and 100 Myr (from left to right). Because DYNAMO galaxies are most similar to $z \sim 1$ galaxies, we expect them to lie between the dotted and dashed model lines for this range of t_{orb}. However, we find that while the shape of the transport+feedback models qualitatively matches DYNAMO, the observed velocity dispersions are still overpredicted.

$\overline{P_{inj}} \propto \Sigma_{0,gas}^{3.8}$ ($\Sigma_{0,gas}$ is the initial gas surface density in each simulation). The authors find that the stronger form of turbulent driving produces a slope of the KS relation more consistent with observations. In addition, they measure the gas velocity dispersion as a function of gas surface density (see their Figure A1). Although the range of gas surface densities probed is small (10–100 $M_\odot$ pc^{-2}), the feedback-only simulation (large-scale turbulent driving turned off) produces small velocity dispersions incompatible with our observations. The weaker turbulent driving simulation ($\overline{P_{inj}} \propto \Sigma_{0,gas}^{2.5}$) with stellar feedback produces the relation

$$\log \sigma_{mol} = 0.65 \times \log \Sigma_{mol} + 0.41 \quad (22)$$

which is steeper than the best-fit slope of $N = 0.47$ that we find (see the left panel of Figure 5). Due to the scatter in the observational measurements, this relation is not inconsistent with the DYNAMO+PHANGS data. However, this weaker turbulent driving simulation produces a steeper slope of the KS relation than is observed. The stronger turbulent driving simulation ($\overline{P_{inj}} \propto \Sigma_{0,gas}^{3.8}$) produces a much steeper relation with a slope of 1.2.

5.1.2. Feedback-regulated Star Formation

In contrast, feedback-regulated models of star formation, which we compare to in the right panel of Figure 7, argue that the primary source of energy in the disk of galaxies is young stars, and the feedback from these stars balances the weight of the ISM (also referred to as pressure-regulated feedback-modulated star formation, PRFM; E. C. Ostriker & C.-G. Kim 2022). Turbulent pressure is maintained by energy/momentum injected from supernovae, and is proportional to the star formation rate per area. Thermal pressure is maintained by photoelectric heating of the gas by stellar far-ultraviolet (FUV) photons and is also proportional to the star formation rate. The disk is then maintained in a state of quasi-equilibrium through a self-regulation of the SFR, such that the energy injected by stellar feedback balances the dissipation of turbulent energy and the cooling of the ISM (see E. C. Ostriker et al. 2010; C.-G. Kim et al. 2011, 2013; E. C. Ostriker & R. Shetty 2011; R. Shetty & E. C. Ostriker 2012; C.-A. Faucher-Giguere et al. 2013; C.-G. Kim & E. C. Ostriker 2015; C. C. Hayward & P. F. Hopkins 2017; M. E. Orr et al. 2018; A. B. Gurvich et al. 2020, for more theoretical details, numerical simulations, and applications).

E. C. Ostriker & C.-G. Kim (2022) revisit this theory and estimate the turbulent, thermal, and magnetic pressures to predict the total feedback yield ($\Upsilon_{tot} = P_{tot}/\Sigma_{SFR}$). They then conduct magnetohydrodynamic simulations within the "Three-phase Interstellar Medium in Galaxies Resolving Evolution with Star Formation and Supernova Feedback" (TIGRESS; C.-G. Kim & E. C. Ostriker 2017) numerical framework to evaluate Υ_{tot} and test the predictions of PRFM theory. The authors use seven TIGRESS simulations that model a three-phase ISM with varying initial gas surface densities in 512×512 pc^2 to 2048×2048 pc^2 galaxy patches and a vertical dimension that is seven times as large. The stellar feedback mechanisms included are supernova explosions and the effects of FUV radiation (see C.-G. Kim et al. 2020, for more details). The authors measure in their simulations feedback yields that are consistent with their theoretical predictions and a $\Sigma_{SFR}-P_{DE}$ relation that is consistent with observations (where P_{DE} is the dynamical equilibrium pressure, an estimate of the ISM weight; see their Figure 15).

To compare our measurements to the results of E. C. Ostriker & C.-G. Kim (2022), we derive an expression relating the gas velocity dispersion to Σ_{SFR} by combining their Equation (28),

$$\frac{\Sigma_{SFR}}{M_\odot \text{ pc}^{-2} \text{ Myr}^{-1}} = 2.07 \times 10^{-4} \frac{P_{DE}/k_B \text{ [cm}^{-3} \text{ K]}}{\Upsilon_{tot} \text{ [km s}^{-1}]}, \quad (23)$$

with an expression for velocity dispersion in their Section 4.6:

$$\sigma = 12 \text{ [km s}^{-1}] \left(\frac{P_{DE}}{10^4 \, k_B \text{ [cm}^{-3} \text{ K]}} \right)^{0.22} \quad (24)$$

and express the velocity dispersion as a function of Σ_{SFR} and Υ_{tot}, the total feedback yield (ratio of the total pressure to Σ_{SFR}):

$$\sigma = 12 \text{ [km s}^{-1}] \left(\frac{1}{2.07} \Sigma_{SFR} \Upsilon_{tot} \right)^{0.22} \quad (25)$$

where Υ_{tot} is given by

$$\Upsilon_{tot} = 740 \text{ [km s}^{-1}] \left(\frac{\Sigma_{SFR}}{0.01 [M_\odot \text{ pc}^{-2} \text{ Myr}^{-1}]} \right)^{-0.18}. \quad (26)$$

Combining these two equations results in the $\sigma_{mol}-\Sigma_{SFR}$ relation

$$\log \sigma_{mol} = 0.1804 \times \log \Sigma_{SFR} + 1.56 \quad (27)$$

which we plot in Figure 7 (solid purple line) and provides reasonable agreement with our DYNAMO measurements. The intercept of $C = 1.56$ predicted by this model is well matched

to what we find for our observations, $C = 1.56 \pm 0.02$, while the slope of $N = 0.1804$ is $\sim 4.5\sigma$ lower than the derived slope for DYNAMO, $N = 0.27 \pm 0.02$.

In the right panel of Figure 7, we also compare to the numerical results from T.-E. Rathjen et al. (2023). This work is built upon the "Simulating the Life Cycle of Molecular Clouds" (SILCC; S. Walch et al. 2015) framework and aims to investigate the effect of cosmic rays on the multiphase structure of star formation-driven outflows. The authors conduct magnetohydrodynamic simulations of the ISM in a $500 \times 500 \times \pm 4000$ pc^3 galactic patch, where they model star formation using sink particles and track the evolution of individual massive stars (8–120 $M_\odot$). Their feedback model includes the effects of core-collapse supernovae, stellar winds, ionizing radiation from massive stars, and cosmic rays. These simulations show that cosmic rays are important for establishing outflows with cold, warm, and hot components. When measuring the velocity dispersion of the cold neutral medium in all simulated environments with cosmic rays, the authors find a power-law relation between $\sigma_{\rm mol}$ and $\Sigma_{\rm SFR}$ of the form

$$\log \sigma_{\rm mol} = (0.20 \pm 0.02) \times \log \Sigma_{\rm SFR} + (1.30 \pm 0.02). \quad (28)$$

This is what we show in the right panel of Figure 7 (purple dashed line) and it also shows good agreement with our resolved DYNAMO measurements. The intercept predicted by this model is much lower than what we find for DYNAMO; as such, the majority of DYNAMO points lie above Equation (28), while the slope of $N = 0.20 \pm 0.02$ is within $\sim 2.5\sigma$ of our measured slope of $N = 0.27 \pm 0.02$. This model also provides a very good match to our fit of the global DYNAMO $\sigma_{\rm mol}$–$\Sigma_{\rm mol}$ relation (see also Figure 2 and Equation (10)).

Finally, we also include as a comparison the stellar feedback-only model of M. R. Krumholz et al. (2018) in the case of fixed Q and variable $\epsilon_{\rm ff}$ (purple dotted line; their Equation (61)):

$$\Sigma_{\rm SFR} = \frac{8(1+\beta)\pi\eta\sqrt{\phi_{\rm mp}\phi_{\rm nt}^3}\,\phi_Q}{GQ^2\langle p_*/m_*\rangle f_{\rm g,P}} \frac{\sigma_{\rm g}}{t_{\rm orb}^2} \quad (29)$$

where $\eta = 1.5$ is a scaling factor for the turbulent dissipation rate, $\phi_{\rm nt} = 1$ is the fraction of the velocity dispersion that is nonthermal, $\phi_Q = 2$ is defined as one plus the ratio of the gas to stellar Q, and all remaining terms are the same as in Equation (19). We have assumed $t_{\rm orb} = 200$ Myr as in the transport+feedback case. Combining this with the additional terms in Equation (29) results in the $\sigma_{\rm mol}$–$\Sigma_{\rm SFR}$ relation

$$\log \sigma_{\rm mol} = 0.5 \times \log \Sigma_{\rm SFR} + 1.81 \quad (30)$$

where the slope of $N = 0.5$ is 11.5σ higher than our best-fit slope. Although the intercept and slope in this case are larger than the best-fit $\sigma_{\rm mol}$–$\Sigma_{\rm SFR}$ relation we find, this model passes reasonably well through the DYNAMO points but underestimates the PHANGS velocity dispersions. Assuming a shorter $t_{\rm orb}$ shifts the M. R. Krumholz et al. (2018) model down (i.e., smaller normalization), which results in poorer agreement with the data. We find similar rms residuals between these three feedback-only models and our data; however, the power-law slopes of the SILCC (T.-E. Rathjen et al. 2023) and TIGRESS (E. C. Ostriker & C.-G. Kim 2022) models are in better agreement with the observed slope measured here.

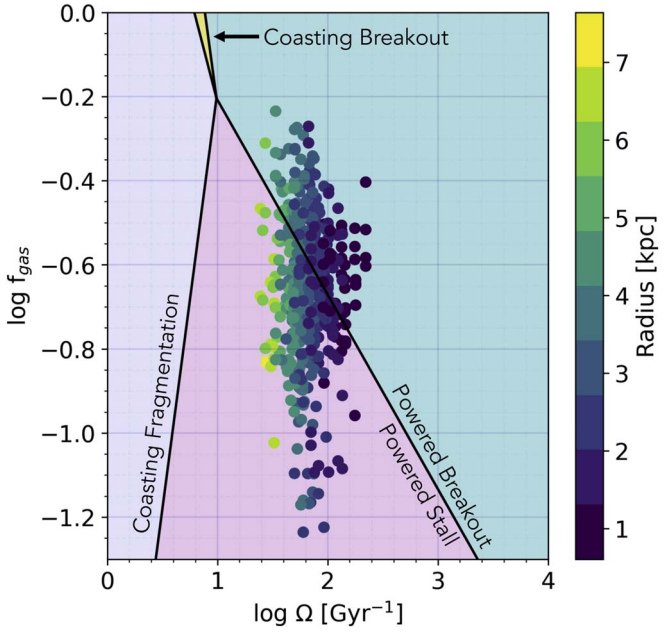

Figure 9. Gas fraction ($f_{\rm gas}$) as a function of orbital frequency ($\Omega = R/V$). The green shaded region of this parameter space is where superbubbles created by clustered supernovae are expected to reach the scale height of the disk and break out to produce outflows before the final supernova goes off ("powered breakout"; M. E. Orr et al. 2022a, 2022b). The pink shaded region is where the superbubble expansion stalls within the disk before reaching the disk scale height and before the final supernova is produced ("powered stall"). DYNAMO line-of-sight measurements (colored circles) are shaded according to the distance of the region from the galaxy center. We find that ∼38% of our DYNAMO measurements lie in the region where outflows and/or fountains are expected to occur.

We conclude from these model comparisons that stellar feedback alone is sufficient to reproduce the $\sigma_{\rm mol}$–$\Sigma_{\rm SFR}$ relation we observe at kiloparsec scales in the gas-rich galaxies of our DYNAMO sample and in the local star-forming PHANGS galaxies.

5.2. Feedback-driven Outflows

M. E. Orr et al. (2022a, 2022b) develop an analytic model to investigate the effects of temporally and spatially clustered supernovae on star formation regulation and the launching of outflows from disk galaxies. Because massive stars only have a short window within which they can undergo a core-collapse supernova (∼40 Myr), the detonation of supernovae is expected to be clustered in space and time and their overlap will create large expanding cavities within the host disk (i.e., a "superbubble"; see also D. Fielding et al. 2018). Such structures are now readily observed in nearby galaxies (with JWST; see, e.g., A. T. Barnes et al. 2023; E. J. Watkins et al. 2023) and in our own Galactic neighborhood (C. Zucker et al. 2022). In the analytical model of M. E. Orr et al. (2022b), superbubbles can expand to reach the scale height of the disk and break out before the last supernova detonates (powered breakout) or after (coasting unpowered breakout). In the breakout case, more than 60% of the feedback momentum can be lost to powering outflows and fountains rather than driving turbulence in the ISM, which results in a reduction of P_*/m_*. Likewise, the superbubble expansion can stall in the ISM before the final supernova (powered stall) or after (coasting

unpowered fragmentation). These four scenarios can be distinguished in gas fraction ($f_{\rm gas}$) versus orbital frequency (Ω) parameter space (see Table 1 in M. E. Orr et al. 2022a, for boundary equations).

We plot $f_{\rm gas}$ versus Ω in Figure 9 with our DYNAMO line-of-sight measurements colored according to their distance from their galaxy center. We find that ∼38% of our measurements lie within the region where powered breakouts, and therefore outflows and/or fountains, are expected to occur. Disk locations as far as ∼6 kpc from their host galaxy center are found in the powered breakout region, suggesting that outflows may be present, and an important star formation regulator, within DYNAMO.

6. Summary and Conclusions

In this work, we have combined ∼1–2 kpc-scale ALMA observations of CO(3−2) and CO(4−3) with HST to study star formation laws in gas-rich star-forming disks. Specifically, we use a sample of seven DYNAMO galaxies to investigate the "molecular gas main sequence," the KS relation, and the relation of molecular gas velocity dispersion to the SFR and molecular gas mass surface densities, which allows us to test theories of star formation regulation. We summarize our findings here.

1. DYNAMO galaxies are more gas-rich than local spirals (see Figure 3) and are not analogous to the centers of local star-forming galaxies. Rather, they lie above the molecular gas main sequence derived from measurements of nearby systems (e.g., EDGE, ALMaQUEST, PHANGS). Our DYNAMO measurements are fit by a shallower slope and larger normalization than what has been found in previous studies of local galaxies.

2. The resolved $\Sigma_{\rm mol}-\Sigma_{\rm SFR}$ relation in DYNAMO galaxies (see Figure 4) has a near linear slope of $N = 0.90 \pm 0.04$ when assuming a fixed, Milky Way–like $\alpha_{\rm CO}$ factor. Under this assumption, more than half of the line-of-sight measurements across our sample have molecular gas depletion times shorter than 1 Gyr. This is in contrast to local galaxies, such as PHANGS and HERACLES, which have median depletion times of ∼2 Gyr. Adopting a variable $\alpha_{\rm CO}$ (Equation (31) in A. D. Bolatto et al. 2013) results in a steeper slope of $N = 1.23 \pm 0.03$. In this case, nearly all positions across the seven DYNAMO disks have depletion times shorter than 1 Gyr.

3. Compared to local galaxies from PHANGS, DYNAMO galaxies have high SFR surface densities, gas surface densities, and velocity dispersions throughout their disks, not just their centers (see Figure 5).

4. We compare our $\sigma_{\rm mol}-\Sigma_{\rm SFR}$ relation to predictions from theories of star formation regulation (see Figure 7) that incorporate stellar feedback and gravitational instabilities as mechanisms for driving turbulence (e.g., M. R. Krumholz et al. 2018), and feedback-regulated star formation theories that invoke stellar feedback alone (e.g., E. C. Ostriker & C.-G. Kim 2022). For the fiducial parameters adopted in M. R. Krumholz et al. (2018), we find that the gravity +feedback model overpredicts $\sigma_{\rm mol}$ when compared to our observations. If we exclude data points where the rotation curves are rising ($\beta \neq 0$), the data sample $t_{\rm orb} = 100$–300 Myr. For these values of $t_{\rm orb}$, the models still overpredict the observed $\sigma_{\rm mol}$ (see Figure 8). Similarly, the large-scale turbulent driving included in the simulations of N. Brucy et al. (2020) produces a $\sigma_{\rm mol}-\Sigma_{\rm mol}$ relation that is steeper than what we observe. In contrast, the magnetohydrodynamic simulations of E. C. Ostriker & C.-G. Kim (2022) and T.-E. Rathjen et al. (2023) predict a relation of $\sigma_{\rm mol} \propto \Sigma_{\rm SFR}{}^{\sim 0.2}$ that provides reasonable matches to both the DYNAMO and PHANGS observations. Finally, the feedback-only model of M. R. Krumholz et al. (2018) predicts $\sigma_{\rm mol} \propto \Sigma_{\rm SFR}{}^{0.5}$ and matches the data reasonably well.

5. Within the $f_{\rm gas}-\Omega$ parameter space, ∼38% of DYNAMO measurements reside in the region where superbubbles resulting from clustered supernovae may break out of the disk and drive outflows and/or fountains (see Figure 9; M. E. Orr et al. 2022a, 2022b).

We conclude that the feedback-regulated models of star formation implemented within the TIGRESS (E. C. Ostriker & C.-G. Kim 2022) and SILCC (T.-E. Rathjen et al. 2023) magnetohydrodynamic simulations reproduce our observations without the need to invoke additional mechanisms for generating turbulence in the ISM such as gas transport or accretion. Both simulation suites (i) model a galactic patch on ∼0.5–1 kpc^2 scales with a vertical dimension that extends several kiloparsecs and physical resolutions of ∼2–8 pc, and (ii) include the effects of supernovae and FUV radiation in their stellar feedback models. SILCC also includes stellar winds and cosmic rays, while TIGRESS models galactic patches within a differentially rotating disk. However, both produce multiphase outflows that are important in regulating star formation and producing results in agreement with observations. While outflows have not been observed in this sample of DYNAMO galaxies, our comparison to the analytical work of M. E. Orr et al. (2022b) suggests they may be present. JWST can be used to map ionized gas tracers in DYNAMO at high resolution, and modeling of the line profiles can be done to search for ionized gas outflows (see, e.g., B. Reichardt Chu et al. 2022a, 2022b).

Acknowledgments

We thank the anonymous referee whose comments have significantly improved this work.

This paper makes use of the following ALMA data: ADS/JAO.ALMA#2017.1.00239.S. and ADS/JAO/ALMA#2019.1.00447.S. ALMA is a partnership of ESO (representing its member states), NSF (USA) and NINS (Japan), together with NRC (Canada), MOST and ASIAA (Taiwan), and KASI (Republic of Korea), in cooperation with the Republic of Chile. The Joint ALMA Observatory is operated by ESO, AUI/NRAO and NAOJ. The National Radio Astronomy Observatory is a facility of the National Science Foundation operated under cooperative agreement by Associated Universities, Inc. Some of the data presented in this article were obtained from the Mikulski Archive for Space Telescopes (MAST) at the Space Telescope Science Institute. The specific observations analyzed can be accessed via doi:10.17909/6dmc-ye91.

L.L. acknowledges support from the NSF through grant 2054178 and acknowledges that a portion of their research was carried out at the Jet Propulsion Laboratory, California Institute of Technology, under a contract with the National Aeronautics and Space Administration (80NM0018D0004).

Parts of this research were supported by the Australian Research Council Center of Excellence for All Sky Astrophysics in 3 Dimensions (ASTRO 3D), through project number CE170100013.

D.B.F. acknowledges support from Australian Research Council (ARC) Future Fellowship FT170100376 and ARC Discovery Program grant DP130101460.

A.D.B. acknowledges support from the NSF under award AST-2108140.

R.C.L. acknowledges support for this work provided by a NSF Astronomy and Astrophysics Postdoctoral Fellowship under award AST-2102625.

J.S. acknowledges support by NASA through the NASA Hubble Fellowship grant HST-HF2-51544 awarded by the Space Telescope Science Institute (STScI), which is operated by the Association of Universities for Research in Astronomy, Inc., under contract NAS 5-26555.

D.O. is a recipient of an Australian Research Council Future Fellowship (FT190100083) funded by the Australian Government.

Facilities: ALMA, HST (ACS, WFC).

Software: aplpy (T. Robitaille 2019), astropy (Astropy Collaboration et al. 2013, 2018, 2022), CASA (J. P. McMullin et al. 2007), numpy (C. R. Harris et al. 2020), reproject (https://reproject.readthedocs.io/en/stable/), SciPy (P. Virtanen et al. 2020), spectral-cube (A. Ginsburg et al. 2019).

Appendix
Discussion of Beam Smearing Correction

To assess the effects of our beam smearing correction discussed in Section 3.4 on our results, we reproduce Figure 5 in Figure A1, where the gray circles correspond to all velocity dispersion measurements with no beam smearing correction applied. The yellow best-fit lines in both panels now correspond to the uncorrected velocity dispersion measurements. In this case, we find a best-fit slope of $N = 0.58 \pm 0.03$ (versus $N = 0.48 \pm 0.02$) for the $\sigma_{\rm mol}-\Sigma_{\rm mol}$ relation, and $N = 0.35 \pm 0.05$ (versus $N = 0.27 \pm 0.02$) for the $\sigma_{\rm mol}-\Sigma_{\rm SFR}$ relation.

As an additional test, we again reproduce Figure 5 in Figure A2; however, we now exclude all velocity dispersion measurements that are within two beams of each galaxy center. Refitting the power laws to this subset of our data, we find best-fit relations that are consistent with what we present in Section 4.4. Therefore, excluding regions where beam smearing will have the greatest impact on the velocity dispersion measurements does not affect or change the results and conclusions.

Finally, in Figure A3, we present the results of our velocity dispersion measurements, corrected for beam smearing, as a function of radius (blue data points), where each panel corresponds to the galaxy indicated in the legend. The black solid line in each panel is the median velocity dispersion in the disk of all points beyond a radius of $1.5\times$ the beam FWHM. For comparison and as a check of our beam smearing correction, the molecular and ionized gas velocity dispersions and uncertainties of M. Girard et al. (2021) are included as the black dashed, black dotted–dashed, and gray shaded regions respectively. The beam FWHM and channel width are represented by the error bars in the top left corner of each panel.

M. Girard et al. (2021) obtained their velocity dispersion measurements from fitting the ALMA rotation curves using GALPAK3D (which corrects for beam smearing; N. Bouché et al. 2015), assuming a flat dispersion model. Beyond the central beam region of each galaxy, our approach using a beam smearing correction produces velocity dispersion results that are consistent with the results of M. Girard et al. (2021): they are all within a channel width or less of each other.

The DYNAMO galaxies in our sample all appear to have higher velocity dispersions in the central beam region than they do in the disk. To assess the significance of this observation, we include as the solid yellow lines the median beam smearing correction, measured in annuli of increasing radius from our model dispersion maps (bottom row, middle panel of Figure 1). Taking into account the channel width and comparing to the median beam smearing correction, it is possible to say that this may be the case for DYNAMO C13-1 and D13-5, and is very likely to be the case for DYNAMO G04-1, G08-5, and G14-1. These three galaxies are the ones for which we use the higher-resolution ALMA observations. This, combined with the turnover radius of the rotation curve of <1 kpc, suggests that the enhanced velocity dispersions we measure at smaller radii are likely real and not a consequence of beam smearing.

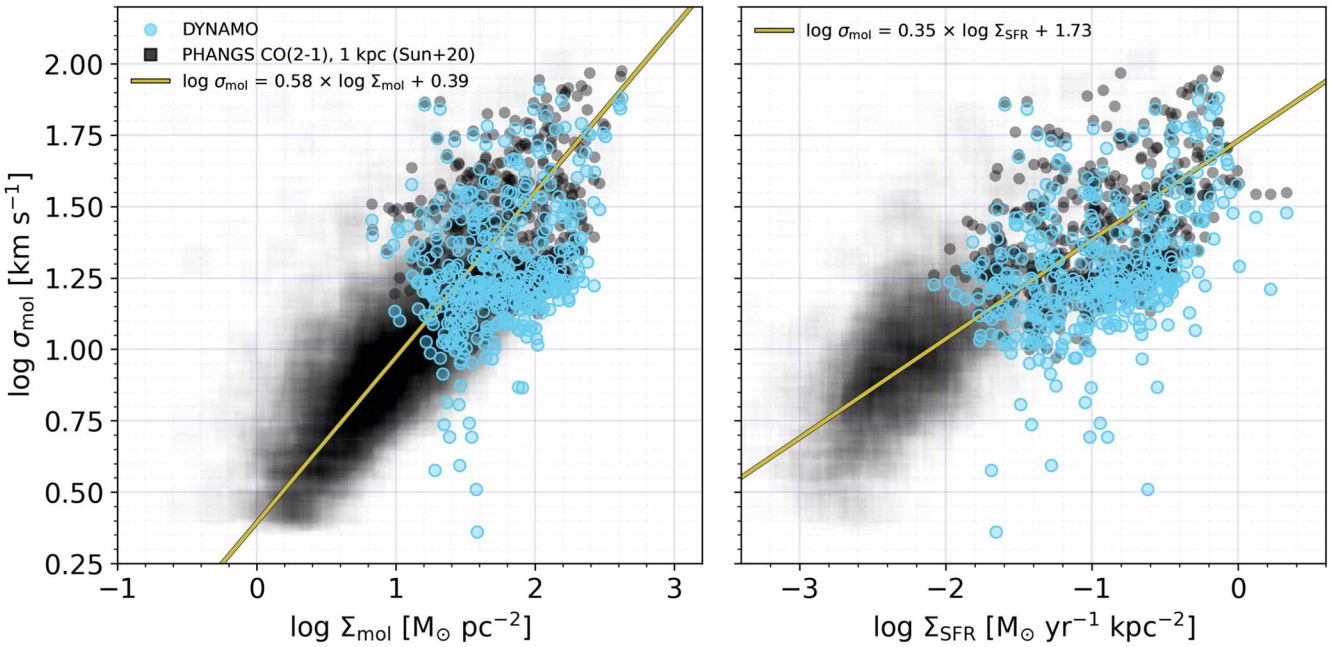

Figure A1. The same as Figure 5; however, we now include the DYNAMO velocity dispersion measurements with no beam smearing correction as gray circles. In this case, we fit the power law to these uncorrected data, and find steeper slopes and best-fit relations that are inconsistent with the best-fit relations presented in Table 2.

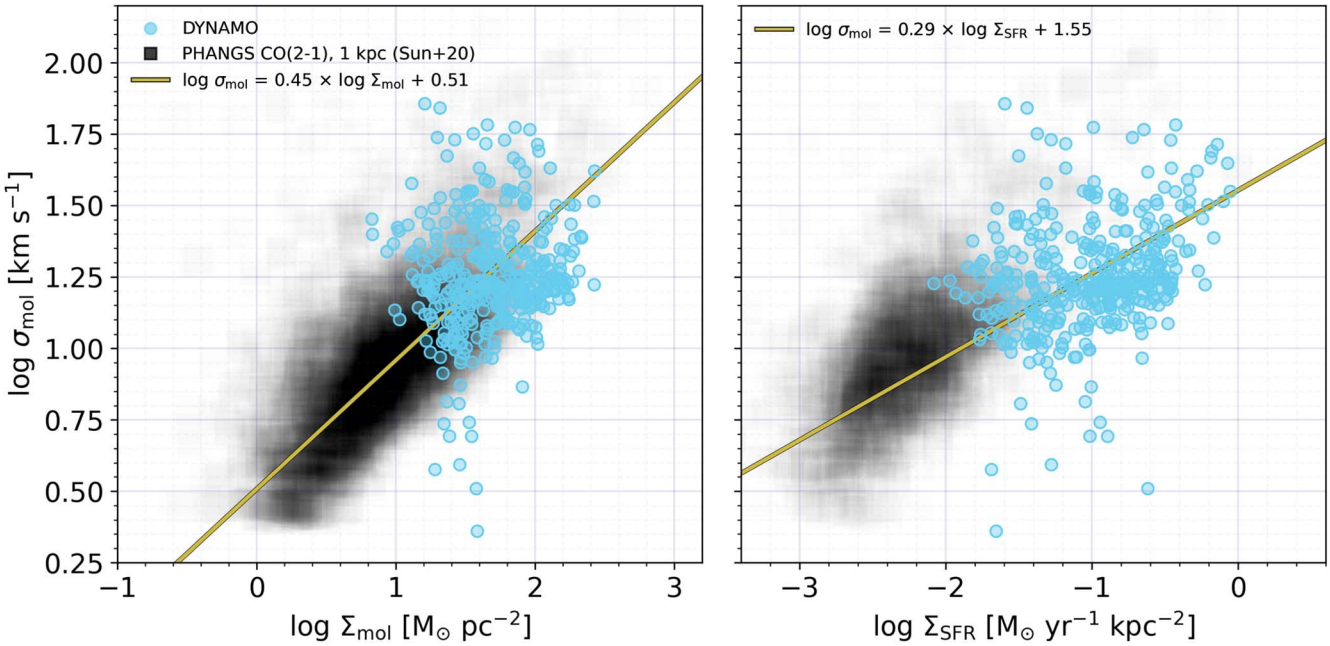

Figure A2. The same as Figure 5; however, we now exclude all beam-smearing-corrected measurements that are within two beams of each galaxy center. When we refit the power laws to this subset of measurements we find results that are consistent with what is presented in Table 2.

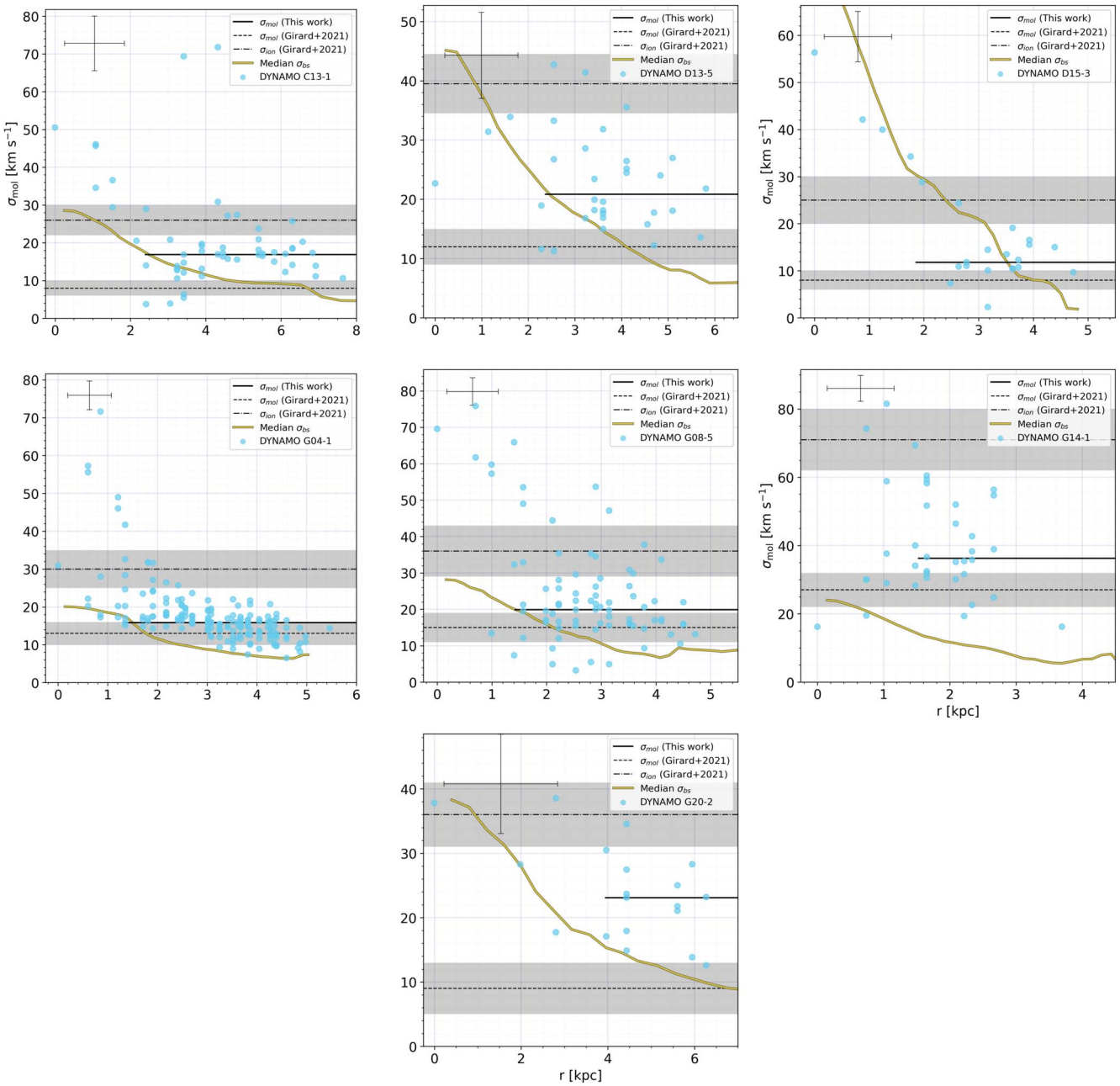

Figure A3. Radial distribution of beam-smearing-corrected velocity dispersion measurements in DYNAMO along beam-sized sightlines (blue data points). The black solid line corresponds to the median velocity dispersion in DYNAMO galaxies at radii larger than 1.5× the beam FWHM. The error bars in the top left corner of each panel indicates the beam FWHM and the channel size of the CO(3−2) observations used to measure velocity dispersions. For comparison, the black dashed and dotted–dashed lines mark the molecular gas and ionized gas velocity dispersion respectively from M. Girard et al. (2021), while the gray shaded region indicates their uncertainties. Within the size of the channel width, our beam-smearing-corrected velocity dispersions are consistent with those found by M. Girard et al. (2021). Finally, the yellow solid line is the radial profile of the median beam smearing correction we apply to each velocity dispersion measurement.

Table 2
Summary of ODR Power-law Fit Results

Relation	Power-law Index, N	Intercept, C
Galaxy-averaged $\sigma_{\rm mol}-\Sigma_{\rm SFR}$	0.19 ± 0.03	1.33 ± 0.04
Resolved $\Sigma_{\rm mol}-\Sigma_{*}$	0.78 ± 0.04	0.05 ± 0.07
Resolved KS law, constant $\alpha_{\rm CO}$, DYNAMO only	0.90 ± 0.04	-2.70 ± 0.08
Resolved KS law, constant $\alpha_{\rm CO}$, DYNAMO+PHANGS	1.04 ± 0.01	-3.15 ± 0.02
Resolved KS law, variable $\alpha_{\rm CO}$, DYNAMO only	1.23 ± 0.03	-3.08 ± 0.06
Resolved $\sigma_{\rm mol}-\Sigma_{\rm mol}$, DYNAMO+PHANGS	0.48 ± 0.02	0.47 ± 0.03
Resolved $\sigma_{\rm mol}-\Sigma_{\rm SFR}$, DYNAMO+PHANGS	0.27 ± 0.02	1.56 ± 0.02
Resolved $\sigma_{\rm mol}-t_{\rm dep}$	-0.80 ± 0.07	1.00 ± 0.03

ORCID iDs

Laura Lenkić https://orcid.org/0000-0003-4023-8657
Deanne B. Fisher https://orcid.org/0000-0003-0645-5260
Alberto D. Bolatto https://orcid.org/0000-0002-5480-5686
Peter J. Teuben https://orcid.org/0000-0003-1774-3436
Rebecca C. Levy https://orcid.org/0000-0003-2508-2586
Jiayi Sun https://orcid.org/0000-0003-0378-4667
Rodrigo Herrera-Camus https://orcid.org/0000-0002-2775-0595
Karl Glazebrook https://orcid.org/0000-0002-3254-9044
Danail Obreschkow https://orcid.org/0000-0002-1527-0762
Roberto Abraham https://orcid.org/0000-0002-4542-921X

References

Ambachew, L., Fisher, D. B., Glazebrook, K., et al. 2022, MNRAS, 512, 3079
Astropy Collaboration, Price-Whelan, A. M., Lim, P. L., et al. 2022, ApJ, 935, 167
Astropy Collaboration, Price-Whelan, A. M., Sipőcz, B. M., et al. 2018, AJ, 156, 123
Astropy Collaboration, Robitaille, T. P., Tollerud, E. J., et al. 2013, A&A, 558, A33
Baker, W. M., Maiolino, R., Belfiore, F., et al. 2023, MNRAS, 518, 4767
Barnes, A. T., Watkins, E. J., Meidt, S. E., et al. 2023, ApJL, 944, L22
Barrera-Ballesteros, J. K., Utomo, D., Bolatto, A. D., et al. 2020, MNRAS, 492, 2651
Bassett, R., Glazebrook, K., Fisher, D. B., et al. 2014, MNRAS, 442, 3206
Begeman, K. G. 1989, A&A, 223, 47
Bigiel, F., Leroy, A., Walter, F., et al. 2008, AJ, 136, 2846
Bolatto, A. D., Wolfire, M., & Leroy, A. K. 2013, ARA&A, 51, 207
Bouché, N., Carfantan, H., Schroetter, I., Michel-Dansac, L., & Contini, T. 2015, AJ, 150, 92
Bournaud, F., Elmegreen, B. G., Teyssier, R., Block, D. L., & Puerari, I. 2010, MNRAS, 409, 1088
Brucy, N., Hennebelle, P., Bournaud, F., & Colling, C. 2020, ApJL, 896, L34
Brucy, N., Hennebelle, P., Colman, T., & Iteanu, S. 2023, A&A, 675, A144
Danovich, M., Dekel, A., Hahn, O., Ceverino, D., & Primack, J. 2015, MNRAS, 449, 2087
Dekel, A., & Burkert, A. 2014, MNRAS, 438, 1870
Dekel, A., Sari, R., & Ceverino, D. 2009, ApJ, 703, 785
Ejdetjarn, T., Agertz, O., Ostlin, G., Renaud, F., & Romeo, A. B. 2022, MNRAS, 514, 480
Ellison, S. L., Lin, L., Thorp, M. D., et al. 2021a, MNRAS, 501, 4777
Ellison, S. L., Wong, T., Sánchez, S. F., et al. 2021b, MNRAS, 505, L46
Elmegreen, B. G., & Burkert, A. 2010, ApJ, 712, 294
Epinat, B., Tasca, L., Amram, P., et al. 2012, A&A, 539, A92
Faucher-Giguere, C.-A., Quataert, E., & Hopkins, P. F. 2013, MNRAS, 433, 1970
Fielding, D., Quataert, E., & Martizzi, D. 2018, MNRAS, 481, 3325
Fisher, D. B., Bolatto, A. D., Glazebrook, K., et al. 2022, ApJ, 928, 169
Fisher, D. B., Bolatto, A. D., White, H., et al. 2019, ApJ, 870, 46
Fisher, D. B., Glazebrook, K., Abraham, R. G., et al. 2017a, ApJL, 839, L5
Fisher, D. B., Glazebrook, K., Bolatto, A., et al. 2014, ApJL, 790, L30
Fisher, D. B., Glazebrook, K., Damjanov, I., et al. 2017b, MNRAS, 464, 491
Förster Schreiber, N. M., Shapley, A. E., Genzel, R., et al. 2011, ApJ, 739, 45
Förster Schreiber, N. M., & Wuyts, S. 2020, ARA&A, 58, 661
Genzel, R., Newman, S., Jones, T., et al. 2011, ApJ, 733, 101
Ginsburg, A., Koch, E., Robitaille, T., et al. 2019, Radio-astro-tools/spectral-cube: v0.4.4, Zenodo, doi:10.5281/zenodo.2573901
Ginzburg, O., Dekel, A., Mandelker, N., & Krumholz, M. R. 2022, MNRAS, 513, 6177
Girard, M., Dessauges-Zavadsky, M., Combes, F., et al. 2019, A&A, 631, A91
Girard, M., Fisher, D. B., Bolatto, A. D., et al. 2021, ApJ, 909, 12
Glazebrook, K. 2013, PASA, 30, e056
Green, A. W., Glazebrook, K., McGregor, P. J., et al. 2014, MNRAS, 437, 1070
Guo, Y., Ferguson, H. C., Bell, E. F., et al. 2015, ApJ, 800, 39
Gurvich, A. B., Faucher-Giguere, C.-A., Richings, A. J., et al. 2020, MNRAS, 498, 3664
Hao, C.-N., Kennicutt, R. C., Johnson, B. D., et al. 2011, ApJ, 741, 124
Harris, C. R., Millman, K. J., van der Walt, S. J., et al. 2020, Natur, 585, 357
Hayward, C. C., & Hopkins, P. F. 2017, MNRAS, 465, 1682
Herrera-Camus, R., Förster Schreiber, N. M., Price, S. H., et al. 2022, A&A, 665, L8
Hopkins, P. F., & Quataert, E. 2011, MNRAS, 415, 1027
Kassin, S. A., Weiner, B. J., Faber, S. M., et al. 2012, ApJ, 758, 106
Kennicutt, R. C., & Evans, N. J. 2012, ARA&A, 50, 531
Kennicutt, R. C., Jr. 1998, ApJ, 498, 541
Kennicutt, R. C., Jr., & De Los Reyes, M. A. C. 2021, ApJ, 908, 61
Kere, D., Katz, N., Weinberg, D. H., & Dave, R. 2005, MNRAS, 363, 2
Kim, C.-G., Kim, W.-T., & Ostriker, E. C. 2011, ApJ, 743, 25
Kim, C.-G., & Ostriker, E. C. 2015, ApJ, 815, 67
Kim, C.-G., & Ostriker, E. C. 2017, ApJ, 846, 133
Kim, C.-G., Ostriker, E. C., & Kim, W.-T. 2013, ApJ, 776, 1
Kim, C.-G., Ostriker, E. C., Somerville, R. S., et al. 2020, ApJ, 900, 61
Klessen, R. S., & Hennebelle, P. 2010, A&A, 520, A17
Kroupa, P. 2001, MNRAS, 322, 231
Krumholz, M. R., & Burkhart, B. 2016, MNRAS, 458, 1671
Krumholz, M. R., Burkhart, B., Forbes, J. C., & Crocker, R. M. 2018, MNRAS, 477, 2716
Law, D. R., Steidel, C. C., Erb, D. K., et al. 2009, ApJ, 697, 2057
Lelli, F., Di Teodoro, E. M., Fraternali, F., et al. 2021, Sci, 371, 713
Lenkic, L., Bolatto, A. D., Fisher, D. B., et al. 2021, MNRAS, 506, 3916
Lenkić, L., Bolatto, A. D., Fisher, D. B., et al. 2023, ApJ, 945, 9
Leroy, A. K., Schinnerer, E., Hughes, A., et al. 2021, ApJS, 257, 43
Leroy, A. K., Walter, F., Bigiel, F., et al. 2009, AJ, 137, 4670
Leroy, A. K., Walter, F., Brinks, E., et al. 2008, AJ, 136, 2782
Leroy, A. K., Walter, F., Sandstrom, K., et al. 2013, AJ, 146, 19
Leung, G. Y. C., Leaman, R., van de Ven, G., et al. 2018, MNRAS, 477, 254
Levy, R. C., Bolatto, A. D., Teuben, P., et al. 2018, ApJ, 860, 92
Lin, L., Pan, H.-A., Ellison, S. L., et al. 2019, ApJL, 884, L33
Liu, D., Förster Schreiber, N. M., Genzel, R., et al. 2023, ApJ, 942, 98
McMullin, J. P., Waters, B., Schiebel, D., Young, W., & Golap, K. 2007, in ASP Conf. Ser. 376, Astronomical Data Analysis Software and Systems XVI, ed. R. A. Shaw, F. Hill, & D. J. Bell (San Francisco, CA: ASP), 127
Molina, J., Ibar, E., Smail, I., et al. 2019, MNRAS, 487, 4856
Obreschkow, D., Glazebrook, K., Bassett, R., et al. 2015, ApJ, 815, 97
Oliva-Altamirano, P., Fisher, D. B., Glazebrook, K., et al. 2018, MNRAS, 474, 522
Orr, M. E., Fielding, D. B., Hayward, C. C., & Burkhart, B. 2022a, ApJL, 924, L28
Orr, M. E., Fielding, D. B., Hayward, C. C., & Burkhart, B. 2022b, ApJ, 932, 88
Orr, M. E., Hayward, C. C., Hopkins, P. F., et al. 2018, MNRAS, 478, 3653
Ostriker, E. C., & Kim, C.-G. 2022, ApJ, 936, 137
Ostriker, E. C., McKee, C. F., & Leroy, A. K. 2010, ApJ, 721, 975
Ostriker, E. C., & Shetty, R. 2011, ApJ, 731, 41
Rathjen, T.-E., Naab, T., Walch, S., et al. 2023, MNRAS, 522, 1843
Reichardt Chu, B., Fisher, D. B., Bolatto, A. D., et al. 2022b, ApJ, 941, 163
Reichardt Chu, B., Fisher, D. B., Nielsen, N. M., et al. 2022a, MNRAS, 511, 5782
Rizzo, F., Bacchini, C., Kohandel, M., et al. 2024, A&A, 689, A273
Rizzo, F., Vegetti, S., Fraternali, F., Stacey, H. R., & Powell, D. 2021, MNRAS, 507, 3952
Robitaille, T. 2019, APLpy v2.0: The Astronomical Plotting Library in Python, v2.0, Zenodo, doi:10.5281/zenodo.2567476
Roman-Oliveira, F., Rizzo, F., & Fraternali, F. 2024, A&A, 687, A35
Romeo, A. B., & Falstad, N. 2013, MNRAS, 433, 1389
Saintonge, A., Kauffmann, G., Kramer, C., et al. 2011, MNRAS, 415, 32
Sánchez, S. F., Barrera-Ballesteros, J. K., Colombo, D., et al. 2021, MNRAS, 503, 1615
Schmidt, M. 1959, ApJ, 129, 243
Shetty, R., & Ostriker, E. C. 2012, ApJ, 754, 2
Sun, J., Leroy, A. K., Ostriker, E. C., et al. 2023, ApJL, 945, L19
Sun, J., Leroy, A. K., Schinnerer, E., et al. 2020, ApJL, 901, L8
Tacconi, L. J., Genzel, R., & Sternberg, A. 2020, ARA&A, 58, 157
Tadaki, K., Iono, D., Yun, M. S., et al. 2018, Natur, 560, 613
Trapp, C. W., Kereš, D., Chan, T. K., et al. 2022, MNRAS, 509, 4149
Tsukui, T., & Iguchi, S. 2021, Sci, 372, 1201
Tsukui, T., Wisnioski, E., Krumholz, M. R., & Battisti, A. 2023, MNRAS, 523, 4654
Übler, H., Genzel, R., Wisnioski, E., et al. 2019, ApJ, 880, 48
Varidel, M. R., Croom, S. M., Lewis, G. F., et al. 2020, MNRAS, 495, 2265
Virtanen, P., Gommers, R., Oliphant, T. E., et al. 2020, NatMe, 17, 261
Wada, K., Meurer, G., & Norman, C. A. 2002, ApJ, 577, 197
Walch, S., Girichidis, P., Naab, T., et al. 2015, MNRAS, 454, 238
Watkins, E. J., Barnes, A. T., Henny, K., et al. 2023, ApJL, 944, L24
White, H. A., Fisher, D. B., Murray, N., et al. 2017, ApJ, 846, 35
Wisnioski, E., Förster Schreiber, N. M., Wuyts, S., et al. 2015, ApJ, 799, 209
Zucker, C., Goodman, A. A., Alves, J., et al. 2022, Natur, 601, 334